
Adsorption and Photocatalytic Decomposition of N₂O on TiO₂(110) and Fe₂(dobdc)

Master thesis

Submitted to fulfill the requirements for the degree of
Master of Science (M.Sc.) in Chemistry

presented by

Marvin Quack

Chair of Physical Chemistry I - Prof. Dr. Karina Morgenstern

Faculty of Chemistry and Biochemistry

Ruhr-University Bochum

September 2015

Contents

| | | |
|----------|---|-----------|
| 1 | Introduction | 1 |
| 2 | Theoretical Principles | 2 |
| 2.1 | Infrared Spectroscopy | 2 |
| 2.1.1 | Basic Principles of Infrared Spectroscopy | 2 |
| 2.1.2 | Molecular Vibration | 3 |
| 2.2 | Nitrous Oxide | 8 |
| 2.2.1 | Chemical Properties of Nitrous Oxide | 8 |
| 2.2.2 | Decomposition of nitrous oxide | 9 |
| 2.3 | Titanium Dioxide | 11 |
| 2.3.1 | Structure of the Rutile TiO ₂ (110) Single Crystal Surface | 11 |
| 2.3.2 | Interaction of TiO ₂ (110) with N ₂ O | 13 |
| 2.4 | Metal-Organic Frameworks | 15 |
| 2.4.1 | Structure of Metal-organic Frameworks | 15 |
| 2.4.2 | Fe ₂ (dobdc) | 15 |
| 2.4.3 | Interaction of Fe ₂ (dobdc) with N ₂ O | 17 |
| 3 | Experimental Section | 19 |
| 3.1 | The FTIR-UHV System | 19 |
| 3.2 | Sample Preparation | 23 |
| 3.2.1 | Preparation of a TiO ₂ (110) Single Crystal | 23 |
| 3.2.2 | Preparation of a Fe ₂ (dobdc) Powder Sample | 24 |
| 3.3 | Adsorption Experiments | 25 |
| 3.4 | UV-light Induced Photoreaction | 26 |
| 4 | Results and Discussion | 27 |
| 4.1 | Reflection-Absorption IR Experiments | 27 |
| 4.1.1 | N ₂ O Adsorption on TiO ₂ (110) | 27 |

| | | |
|----------|---|-----------|
| 4.1.2 | Thermal Desorption of N ₂ O | 31 |
| 4.1.3 | Photoreaction of N ₂ O on TiO ₂ (110) | 32 |
| 4.2 | Transmission UHV-FTIR Experiments | 37 |
| 4.2.1 | Probing the Adsorption Sites of Fe ₂ (dobdc) with CO | 37 |
| 4.2.2 | N ₂ O Adsorption on Fe ₂ (dobdc) | 38 |
| 5 | Conclusion | 42 |
| 5.1 | Adsorbed N ₂ O on Rutile TiO ₂ (110) | 42 |
| 5.2 | Adsorbed N ₂ O on Fe ₂ (dobdc) | 42 |

List of Figures

| | | |
|------|--|----|
| 2.1 | Potential energy diagram of the quantum harmonic oscillator | 4 |
| 2.2 | Potential energy diagram of the Morse oscillator | 6 |
| 2.3 | The four different vibrational modes of CO ₂ | 7 |
| 2.4 | The two possible resonance structures of N ₂ O | 8 |
| 2.5 | Decomposition reactions of N ₂ O | 10 |
| 2.6 | The (110) surface of α -TiO ₂ | 12 |
| 2.7 | Adsorption geometry of N ₂ O at the defect-free TiO ₂ (110) surface | 14 |
| 2.8 | Three-dimensional structure of MOF-5 | 15 |
| 2.9 | Three-dimensional structure of Fe ₂ (dobdc) | 16 |
| 2.10 | Calculated structures for adsorbed N ₂ O at Fe ₂ (dobdc) active sites. | 17 |
| 3.1 | Schematical setup of the UHV-FTIR system | 20 |
| 3.2 | Schematical setup of the sample holder | 22 |
| 3.3 | Schematical setup of the IR beam path | 23 |
| 4.1 | UHV-FTIR spectra of the α -TiO ₂ (110) single crystal surface at 102 K | 28 |
| 4.2 | UHV-FTIR spectra of the α -TiO ₂ (110) single crystal surface after N ₂ O dosing at different temperatures. | 30 |
| 4.3 | UHV-FTIR spectra of the α -TiO ₂ (110) single crystal at different temperatures during annealing | 32 |
| 4.4 | UHV-FTIR spectra of the α -TiO ₂ (110) single crystal surface at 102 K during UV irradiation | 33 |
| 4.5 | Time-dependent N ₂ O depletion diagrams | 34 |
| 4.6 | UHV-FTIR spectra of the Fe ₂ (dobdc) powder sample during CO exposure at 95 K | 37 |
| 4.7 | UHV-FTIR spectra of the Fe ₂ (dobdc) powder sample during N ₂ O exposure at 95 K | 39 |
| 4.8 | UHV-FTIR spectra of the Fe ₂ (dobdc) powder sample during annealing | 40 |

1 Introduction

Despite the low concentration of nitrous oxide in atmosphere compared to other greenhouse gases, like carbon dioxide (CO_2) or methane (CH_4), N_2O is one of the main reasons for global warming with a global warming potential, which is about 300 times higher than that of CO_2 .^{1,2} In addition, N_2O is known to be responsible for stratospheric ozone depletion.³

To decrease the emission of N_2O , a possible approach is the catalytic decomposition into molecular nitrogen and oxygen. In recent years, a lot of effort has been made to understand the decomposition mechanisms in detail in order to create novel catalyst systems with better activity towards N_2O decomposition.⁴⁻⁶ While thermal catalysts are mostly restricted to waste gas cleaning in industrial plants,⁵ photocatalysts, capable of N_2O dissociation using sunlight as an energy source, are an energy and cost efficient solution to reduce the greenhouse gas emission.⁷

A catalyst system that has been extensively studied, is titanium dioxide.⁸ While it has been shown that N_2O dissociates into molecular nitrogen and an adsorbed oxygen atom at $\text{TiO}_2(110)$ surfaces under UV irradiation, the mechanism of this reaction is not fully understood. In particular, the role of oxygen defects (V_{O} s) is highly discussed and different possible reaction mechanisms are proposed.^{14,20?}

Another system that shows activity towards N_2O decomposition is the metal organic framework (MOF) $\text{Fe}_2(\text{dobdc})$ ($\text{dobdc} = 2,5\text{-dioxido-1,4-benzenedicarboxylate}$).⁹ The defect-free framework with easy accessible metal centers inside the pores features possible adsorption sites for different small molecules. Recently, it has been shown that the catalytic oxidation of ethane to ethanol is driven by N_2O dissociation to give a Fe(III)-oxo species capable of C-H bond activation.

The aim of this work is to get a better understanding of the decomposition process of N_2O on different surfaces. For that, the interaction of N_2O on an oxidized rutile $\text{TiO}_2(110)$ single crystal and a $\text{Fe}_2(\text{dobdc})$ powder sample has been studied by UHV-FTIR spectroscopy.

2 Theoretical Principles

The first part of this chapter describes the basic principles of FTIR spectroscopy and the underlying concept of molecular vibration. In the second part, the properties of nitrous oxide and its decomposition mechanisms are summarized. Further, the surface properties of the examined substrates, namely a rutile TiO₂(110) single crystal and a Fe₂(dobdc) powder sample, and their interaction with nitrous oxide are explained.

2.1 Infrared Spectroscopy

2.1.1 Basic Principles of Infrared Spectroscopy

The basic principle of infrared spectroscopy, or spectroscopy in general, is the interaction of electromagnetic radiation with a sample.¹⁰ Depending on the energy of the incident photons, different processes can occur:

1. The absorption of photons leads to excitation of the sample, as for example to electronic excitation from binding to antibinding molecular orbitals (UV/Vis spectroscopy or vibrational and rotational excitation of atoms and molecules (IR spectroscopy)).
2. The irradiation induces the emission of electromagnetic radiation (emission spectroscopy, ES).
3. The incident photons are scattered at the sample and give information about the periodic structure of the molecules or surfaces (X-ray diffraction, XRD).

The energy of an absorbed or emitted photon is related to the corresponding excitation energy ΔE and is defined by its frequency ν or its wavelength λ :

$$\Delta E = h \cdot \nu = \frac{h \cdot c}{\lambda}. \quad (1)$$

h: Planck constant ($h = 6.62606957 \cdot 10^{-34} \text{ J}$)

c: Speed of light in vacuum ($c = 2.998 \cdot 10^8 \text{ m} \cdot \text{s}^{-1}$)

In case of IR spectroscopy, absorption of photons mainly leads to vibrational and rotational excitation of molecules.¹¹ Based on its wavelength, IR radiation is divided into near (800 - 2500 nm), mid (2500 - 50000 nm) and far (50000 - 1000000 nm) infrared. To characterize the vibrations of molecules, mainly mid-IR radiation is used, since its energy is in the range of vibrational normal modes of most functional groups, whereas the absorption of near-IR primarily excites the vibration of hydrogen-containing groups and overtone vibrations.¹²

2.1.2 Molecular Vibration

The simplest model to describe molecular vibration of diatomic molecules is the harmonic oscillator (HO), in which the bond between the two atoms with the mass m_1 and m_2 behaves like an elastic spring with a force constant k .¹⁰ According to Hooke's law, the repulsive force is proportional to the deflection from the equilibrium distance r_e . The resulting potential energy in dependence of the atomic distance r can be described with a parabolic potential energy curve:

$$V(r)_{HO} = \frac{1}{2} \cdot k(r - r_e)^2. \quad (2)$$

Due to quantum mechanics, the potential energy is quantized and vibrational energy levels can only take discrete values. The solution of the Schrödinger equation for this potential gives the allowed energy eigenvalues E_n of the harmonic oscillator as a function of the vibrational quantum number n .

$$E_n = n + \frac{1}{2} h \cdot \nu. \quad (3)$$

n : vibrational quantum number (0, 1, 2, ...)

h : Planck's constant ($6.62618 \cdot 10^{-34} [Js]$)

ν : vibrational frequency [s^{-1}]

Equation 3 shows that even at the vibrational ground state ($n = 0$), the molecule has an energy of $E_0 = \frac{1}{2}h\nu$, which describes the energy of a system at absolute zero. The vibrational frequency is dependent on the atomic masses m_1 and m_2 of the molecule as well as on the force constant k , given by:

$$\nu = \frac{1}{2\pi} \sqrt{\frac{k}{\mu}} \quad \text{with} \quad \mu = \frac{m_1 m_2}{m_1 + m_2}. \quad (4)$$

μ : reduced mass [kg]

m_1, m_2 : masses of atoms in a diatomic molecule [kg]

k : force constant [$\frac{kg}{s^2}$]

The potential energy diagram for the quantum harmonic oscillator is shown in Figure 2.1. The energy levels of the harmonic oscillator are equidistant and only transitions with $\Delta n = \pm 1$ are allowed. Although this model is sufficient to describe the vibrational excitation in proximity to the equilibrium distance, the description of larger deflections is not realistic, since it does not include a possible dissociation of the molecule for large atomic distances. In contrast to the model of the harmonic oscillator, a possible bond

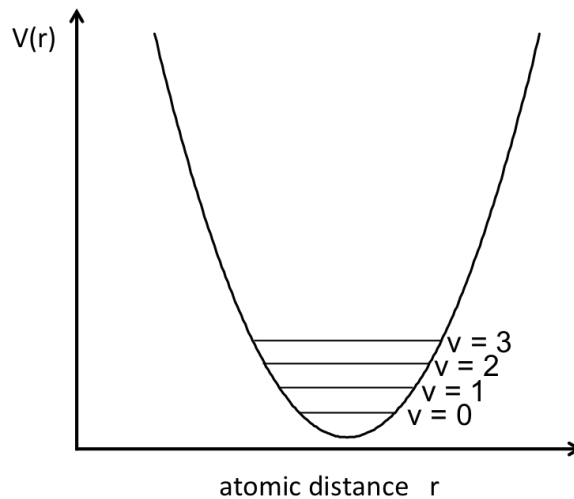


Figure 2.1: Potential energy diagram of the quantum harmonic oscillator.

breaking is included in the model of the anharmonic oscillator (AO). Commonly, the

anharmonic Morse potential is used to give a more realistic description for the vibration of a diatomic molecule.¹⁰

$$V(r)_{AO} = D_e \cdot (1 - e^{\alpha(r-r_e)})^2 \quad (5)$$

D_e : spectroscopic dissociation energy [J]

α : molecule specific constant [m^{-1}]

The energy eigenvalues are given by:

$$E_n = (n + \frac{1}{2})h\nu - (n + \frac{1}{2})^2 \chi h\nu \quad (6)$$

χ : anharmonicity constant

In the anharmonic oscillator, the energy levels are no longer equidistant and the distance decreases for larger vibrational quantum numbers to reach an energy continuum at which the molecule dissociates. Moreover, also transitions of more than one energy level ($\Delta n = \pm 2, \pm 3, \dots$) - so called overtones - are allowed. The potential energy diagram of the Morse oscillator is shown in Figure 2.2.

The motional degrees of freedom have to be considered to determine the possible vibrational modes of a molecule and, thereby, the signals in the corresponding IR spectrum: A molecule containing N atoms has $3 \cdot N$ degrees of freedom, describing the translational, rotational and vibrational motion.¹⁰ The translational motion of the molecule in three-dimensional space takes three degrees of freedom, one for each spatial direction, which cannot be counted to the vibrational degrees of freedom. Another three degrees of freedom describe the rotational motion of a non-linear molecule about its axes. However, in a linear molecule only two degrees of freedom are needed, because the rotation about the molecular axis does not result in a displacement of the atoms within the molecule. This gives $3N-6$ vibrational degrees of freedom for non-linear, and $3N-5$ degrees of freedom for linear molecules, called vibrational normal modes. The vibrational normal modes

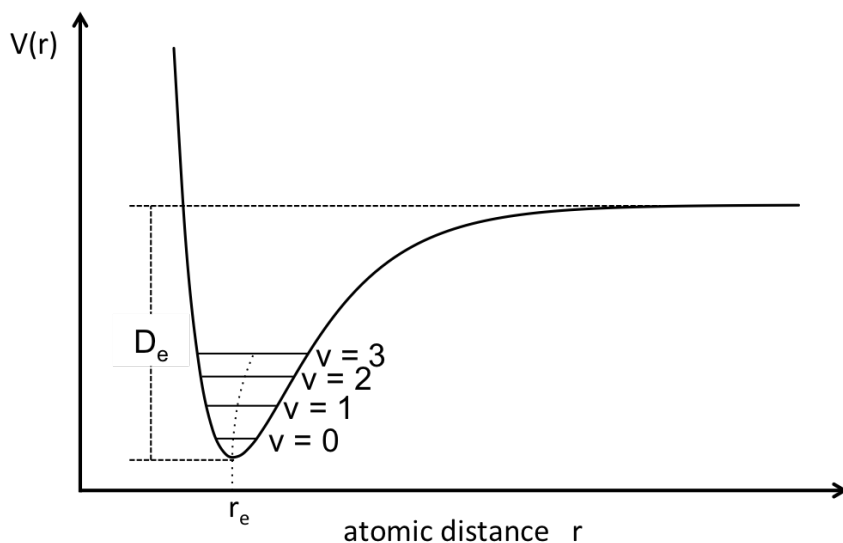


Figure 2.2: Potential energy diagram of the Morse oscillator.

can be separated into stretching modes that cause a change of the bond length of the atoms within a molecule, and bending modes that lead to a change in the bonding angle. Furthermore, a distinction is made between symmetric and asymmetric vibrations.

To be detectable with IR measurements, the vibrational excitation requires a change in the dipole moment of the molecule.¹³ A permanent dipole is not necessary, since the vibration can change the dynamic dipole moment of the molecule during irradiation. However, in homodiatomic molecules, like N_2 or H_2 , the dipole moment is always zero, independent from the bond length. Therefore, homodiatomic molecules are IR inactive, whereas heterodiatomic molecules are always IR active. In larger molecules, different vibrational modes can cause a change in the dipole moment of the molecule and can be detected in IR measurements. However, not every vibration leads to a change in dipole moment and can be seen in IR spectra, which can be explained on a simple molecule like CO_2 . Figure 2.3 shows the four possible vibrational modes of CO_2 . The symmetric stretching mode (a) is IR inactive, since it does not cause a change in the dipole moment of the molecule. In contrast, the asymmetric stretching vibration (b) as well as the two degenerate bending modes of the molecule (c) lead to a change in the dipole moment and are, therefore, IR active. However, the two bending modes have the same energy and

the resulting IR spectrum shows only two signals - one from the asymmetric stretching mode and one from the bending modes.

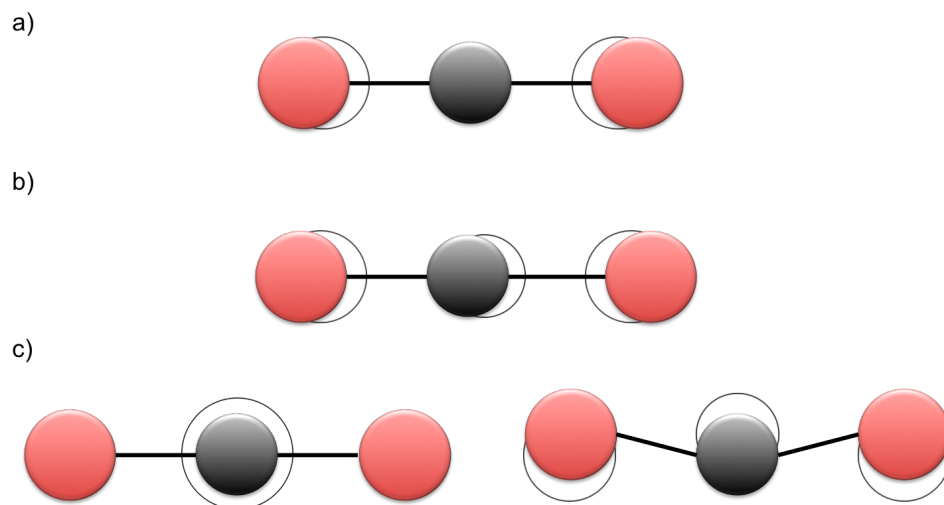


Figure 2.3: The four different vibrational modes of CO_2 : a) the IR-inactive symmetric stretching mode, b) the IR-active asymmetric stretching mode and c) the two IR-active degenerate bending modes. O: red spheres, C: grey spheres.

2.2 Nitrous Oxide

2.2.1 Chemical Properties of Nitrous Oxide

At room temperature, nitrous oxide is a colorless, non-toxic and non-flammable gas with the chemical formula N_2O and a linear molecule structure.¹⁴ The N-N bond length amounts to 112.6 *pm*, while the N-O bond is longer with 118.6 *pm*. The resonance structures of N_2O are shown in Figure 2.4. The molecule has a molar mass of 44.01 *g/mol* and a dipole moment of 0.16 *D*.

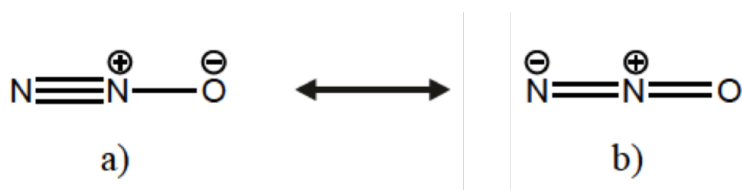


Figure 2.4: The two possible resonance structures of N_2O a) with the negative charge at the O atom and b) with the negative charge at the N atom.

Nitrous oxide, commonly known as laughing gas, was first discovered and isolated in 1772 by Joseph Priestley during his studies of gases.¹⁵ A general interest in nitrous oxide arose after the chemist Humphry Davy observed the pain-relieving effect upon inhalation of the substance in a self-experiment in 1799. These findings later inspired the dentist Horace Wells to use nitrous oxide during tooth extractions to reduce the pain of the patients during the surgery.¹⁶ Nowadays, nitrous oxide is not only one of the most commonly used pain-relieving substances in medicine, but is also used as a food additive, for example in whipped cream dispensers, or as additional oxygen source in combustion engines.

During the last decades, however, the negative effects of atmospherical N_2O have been discussed.^{1-3,7,17} Despite its low concentration, the long lifetime of 113 years and the high IR absorption efficiency make N_2O a greenhouse gas with a global warming potential about 300 times higher than that of carbon dioxide.¹ In addition, N_2O is known to be the primary source of stratospheric NO_x species that cause the depletion of the ozone layer.¹⁷ Therefore, N_2O is the third most important greenhouse gas after carbon dioxide

and methane regarding its contribution to global warming.

Today, approximately 65 % of the total N₂O emission is based on natural sources, like soils and oceans, where it is a product of microbial processes in the global nitrogen cycle. The other 35 % rise from anthropogenic sources, such as chemical industry, fossil fuel combustion and agricultural soils.¹⁸ A possibility to reduce the N₂O emission is the decomposition into O₂ and N₂.

2.2.2 Decomposition of nitrous oxide

The thermal decomposition of N₂O proceeds at high temperatures ($> 800^{\circ} C$) in an exothermic reaction ($\Delta_r H_m^{\ominus}(T = 298 K) = -163 kJ/mol$).⁵ To avoid the incomplete conversion of N₂O into NO_x species, the reaction is usually carried out in fixed-bed reactors over an inert packing material to maintain constant temperatures. In order to improve the selectivity and lower the activation energy of the reaction, the catalytic decomposition of N₂O has been intensively studied on various metal¹⁹ and metal oxide catalysts as well as on zeolites.^{5,8} In general, the catalytic reaction requires the adsorption of N₂O on an active center on the catalyst surface, which is followed by the dissociation of the molecule into gaseous nitrogen and an oxygen atom adsorbed on the catalyst surface. Molecular oxygen is then formed by recombination with another adsorbed oxygen atom or by the direct reaction with another N₂O molecule. The two reaction pathways for the decomposition of N₂O are shown in Figure 2.5.

While thermal catalytic decomposition of N₂O still requires elevated temperatures and is mostly restricted to processes like waste gas treatment in industry or combustion engines, photocatalytic decomposition can be applied to reduce the N₂O emission of other sources at room temperature or even below.

The irradiation of photocatalysts with light in the UV range excites electrons from the valence band into the conduction band of a semiconductor, if the energy of the incident photons is larger than the band gap. The excited electrons can reduce adsorbed nitrous oxide to N₂ and an oxygen atom adsorbed on the surface of the catalyst.²⁰ Different photocatalysts have shown activity towards N₂O decomposition, but due to its

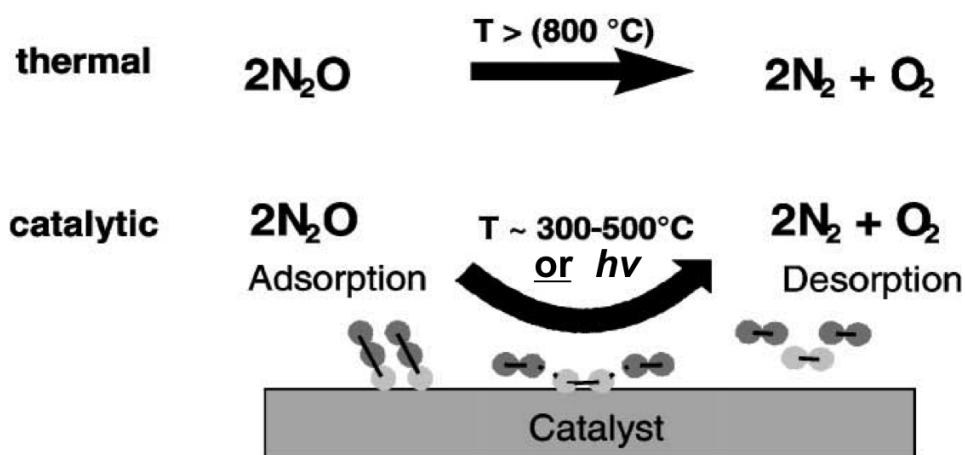


Figure 2.5: The pathways of thermal and catalytic N_2O decomposition. The mechanism of the catalytic reaction is shown schematically. Taken from 5.

well-known structure and properties, TiO_2 is one of the most studied photoactive metal oxides in this field.^{2,4,7,19-25}

In 2008, a first field experiment has successfully shown that coating the walls of a pig stall with TiO_2 nanoparticles reduces the concentration of N_2O under the irradiation with sunlight at room temperature. It is notable, that the focus in this experiment was based on ammonia decomposition and the TiO_2 nanoparticles have not been modified to increase the activity towards N_2O decomposition.⁷

In order to understand the photocatalytic activity of TiO_2 towards N_2O decomposition, the physical and chemical properties of TiO_2 as well as the interaction with N_2O are explained in the following.

2.3 Titanium Dioxide

Titanium dioxide is a non-toxic metal oxide semiconductor with the stoichiometric formula TiO_2 .^{8,26} In nature, TiO_2 crystallizes in three different modifications, namely rutile, anatase and brookite, while anatase and brookite are thermodynamically meta-stable and are irreversibly converted to rutile at temperatures above 600 °C. In fact, the chemically stable rutile is the most studied modification with regard of catalytic applications.^{8,27} In addition, eight synthesized modifications of TiO_2 are known.

Because of its chemical and thermal stability as well as its interesting properties, several applications of TiO_2 are found in various fields. It is used in heterogeneous catalysis and photocatalysis²⁸⁻³⁰ as well as for solar cells. As a white pigment, it is also used in paints, corrosion-protective coatings for different materials or even as food additive. Rutile TiO_2 single crystals as well as nanoparticles are commercially available with different surface orientations and particle sizes.

In its most stable rutile modification, also called α - TiO_2 , the crystal structure consists of threefold coordinated O^{2-} and sixfold coordinated Ti^{4+} ions in a tetragonal lattice.²⁷ The low-index surfaces of the crystal are (110), (100) and (001). The stability of these three surfaces has been calculated by theoretical *ab initio* calculations. The most stable surface is the (110) surface followed by the (100) surface, while the (001) surface is unstable and reconstructs to form a (1x1)(011) surface.

2.3.1 Structure of the Rutile $\text{TiO}_2(110)$ Single Crystal Surface

The rutile $\text{TiO}_2(110)$ surface (Fig. 2.6) has been extensively studied and the structural properties of the surface are well-known.⁸ The perfect surface consists of two types of Ti atoms in alternating rows along the (001) direction. The sixfold coordinated Ti atoms (Ti_6) are comparable with Ti atoms in the bulk, whereas the fivefold coordinated Ti atoms (Ti_5) are undercoordinated and have one dangling bond perpendicular to the surface. On top of the Ti_6 rows are bridging oxygen atoms, which are twofold coordinated, while threefold coordinated oxygen rows are in-plane with the Ti atoms. The autocompensation of the surface charge, due to the same number of undercoordinated oxygen

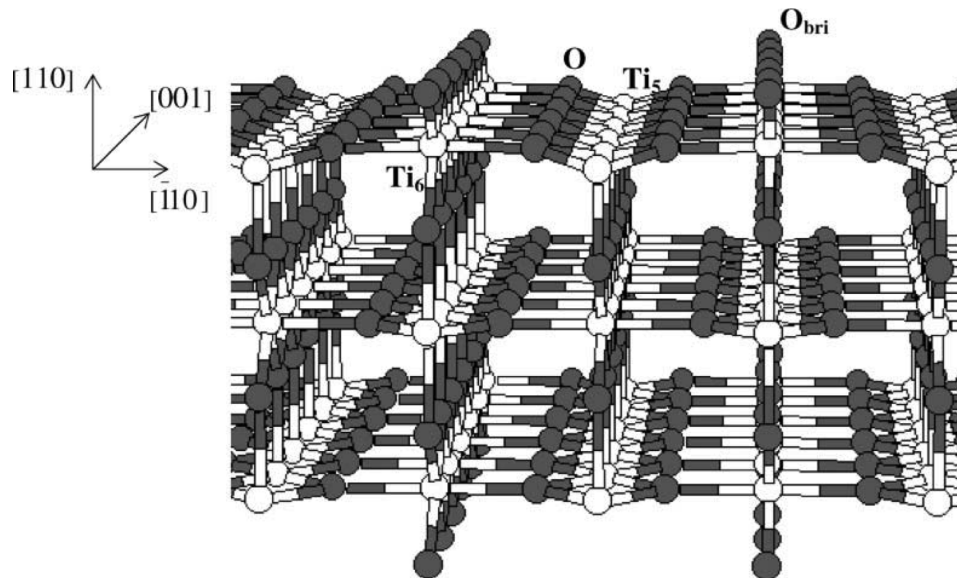


Figure 2.6: The perfect (110) surface of α -TiO₂. The fivefold and sixfold coordinated Ti atoms (grey spheres) are labeled as Ti₅ and Ti₆, respectively. The oxygen atoms (white spheres) are labeled as O for threefold coordinated oxygen and O_{bri} for bridging oxygen atoms on top of the surface. The crystallographic axes are represented. Taken from 27.

and titanium atoms, results in a net charge of the surface equal to zero.²⁷ With regard to the bulk, the TiO₂(110) surface structure is slightly distorted. The Ti₆ rows on the surface move upwards, while Ti₅ atoms move downwards, resulting in a relaxation of the surface.

However, during the preparation of TiO₂ single crystal surfaces for experimental studies, the crystal structure can be altered by different processes, as for example during heating or ion bombardment of the sample. The resulting defects in the bulk and on the surface structure influence the chemical and catalytic properties of TiO₂. Especially surface oxygen vacancies are known to play an important role as active centers in different catalytic reactions, as they partially reduce the surface.³¹ On an α -TiO₂(110) surface two types of oxygen vacancies are possible - missing oxygen atoms from the surface layer and missing bridging oxygen atoms. In both cases, oxygen vacancies convert Ti₆ into Ti₅ species leading to a reduction of the surface, but only bridging oxygen vacancies expose Ti atoms to the surface making them accessible for catalytic reactions.

2.3.2 Interaction of TiO₂(110) with N₂O

In 1997, Schultz et al. have used X-ray photoelectron emission spectroscopy (XPS) and second harmonic generation (SHG) to show that N₂O heals oxygen vacancies on a TiO₂(110) single crystal surface under UV irradiation to give molecular nitrogen and an oxygen atom adsorbed to the surface.³² Based on these findings, the reaction of N₂O with TiO₂ has been studied intensively and the photocatalytic activity of N₂O decomposition has been verified by different surface analytic techniques as well as with theoretical calculations.

The interaction of N₂O with TiO₂ nanoparticles has been studied by Rusu et al. using transmission UHV-FTIR spectroscopy.²⁰ The measurements confirmed the existence of two differently adsorbed N₂O species on the TiO₂ nanoparticles at 157 K, which are assigned to O-bonded and N-bonded N₂O at the metal centers of the sample. During UV irradiation, the depletion of the N₂O vibrational modes in the IR spectra is observed, caused either by photocatalytic desorption or by photocatalytic dissociation of N₂O. The active species in both cases is the N-bonded N₂O species, while the O-bonded species is not affected by UV irradiation. At low initial N₂O coverages, mainly photoactive dissociation of the N-bonded species takes place resulting in the formation of molecularly adsorbed N₂ and an adsorbed O²⁻ ion at the surface. At high coverages, only photocatalytic desorption is observed.

Temperature programmed desorption (TPD) studies, as well as X-ray photoelectron spectroscopy (XPS) and high-resolution electron energy loss spectroscopy (HREELS) of N₂O adsorbed at a rutile TiO₂ single crystal during UV irradiation show similar results and have been published by Henderson et al.⁶ Two peaks in the TPD spectra are observed at 130 and 170 K, which are assigned to O-bonded and N-bonded N₂O species, respectively. The O-bonded species is weakly bound and desorbs from the surface at around 130 K. However, the N-bonded species decomposes at 170 K under release of N₂ and the adsorption of an O²⁻ at non-defect Ti⁴⁺ sites. In addition, the photoactive dissociation of the O-bonded species at 90 K is observed to result in N₂ formation and the oxidation of vacancy sites at the surface. Both decomposition reactions are believed

to be vacancy-mediated.

Oviedo et al. studied the adsorption geometry of N_2O at oxidized and reduced rutile $\text{TiO}_2(110)$ single crystal surfaces by the use of density functional theory (DFT) and molecular dynamic (MD) simulations.³³ The results show that N_2O adsorbs at the surface either *via* the O-end or the N-end of the molecule in a linear configuration (Fig. 2.7. The N-bonded species remains perpendicular to the surface even after long simulation times, whereas the O-bonded N_2O is tilted. Furthermore, the dissociation of N_2O has been found to occur only at the reduced surface indicating that the process is vacancy-mediated as proposed by experimental studies.

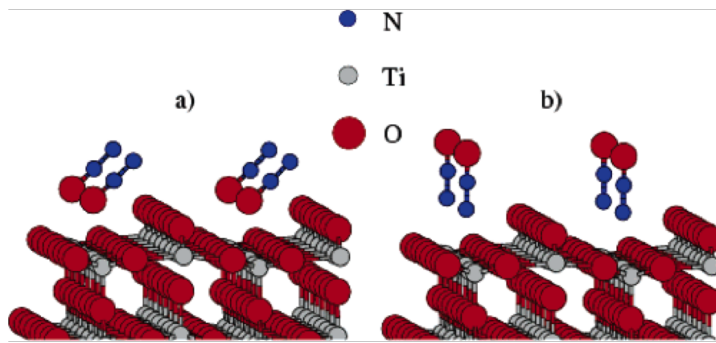


Figure 2.7: Adsorption geometry of a) O-bonded and b) N-bonded N_2O at the defect-free $\text{TiO}_2(110)$ surface based on MD simulations. Taken from 33.

However, a rather recent study by Kim et al. shows that the adsorption of N_2O on a partially reduced $\text{TiO}_2(110)$ surface does not result in N_2O decomposition during TPD measurements.¹⁴ In contrast to prior experiments, no dissociation is observed at 170 K and another peak at 175 K is assigned to the photodesorption of vacancy-bonded N_2O .

In this work, the photocatalytic activity of an oxidized $\text{TiO}_2(110)$ single crystal surface towards N_2O decomposition is investigated by UHV-FTIR measurements to get better understanding of the possible depletion mechanisms. In addition, the results can help to explain the role of oxygen vacancies with regard to the decomposition of N_2O .

2.4 Metal-Organic Frameworks

2.4.1 Structure of Metal-organic Frameworks

Another class of molecules showing promising activity towards the dissociation of small molecules, like N_2O , are metal organic frameworks (MOFs).^{9,34-39} The crystalline structure of MOFs is based on coordinated metal clusters, so called secondary building units (SBUs), that are linked to each other by organic linker molecules, producing a stable nanoporous structure with a high surface area.³⁵ Figure 2.8 shows the structure of MOF-5 as a prototype of MOFs with a primitive cubic crystal system based on octahedral Zn_4O SBUs linked by bridging terephthalate linkers. By using SBUs with different geometries and varying the size of the linkers, a large number of MOFs with various crystal structures and pore sizes can be synthesized, which show interesting applications in gas storage and separation as well as catalysis.⁴⁰

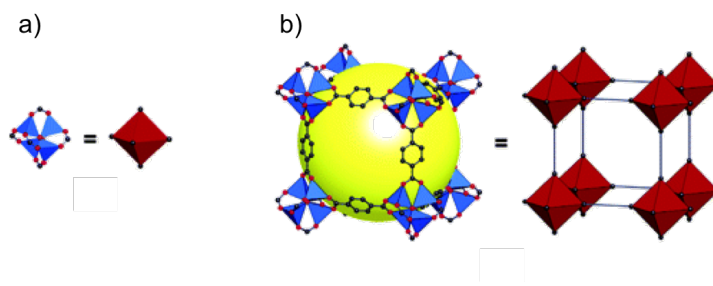


Figure 2.8: Three-dimensional structure of MOF-5: a) Octahedral metal-carboxylate SBU, b) SBUs linked by benzene units to produce a three-dimensional, primitive cubic crystal structure. O: red spheres, C: grey spheres, Zn: blue triangles. Taken from 35.

2.4.2 $\text{Fe}_2(\text{dobdc})$

An interesting compound that exhibits coordinatively unsaturated Fe(II) active centers, which are capable of N_2O decomposition, is the MOF $\text{Fe}_2(\text{dobdc})$, also known as Fe-MOF-74.⁹ The framework consists of helical chains of Fe(II) ions connected by the carboxylate groups of 2,5-dioxido-1,4-benzenedicarboxylate (dobdc^{4-}) to give a three-dimensional structure with hexagonal channels (Fig. 2.9) and a surface area of $1360 \text{ m}^2 \cdot \text{g}^{-1}$

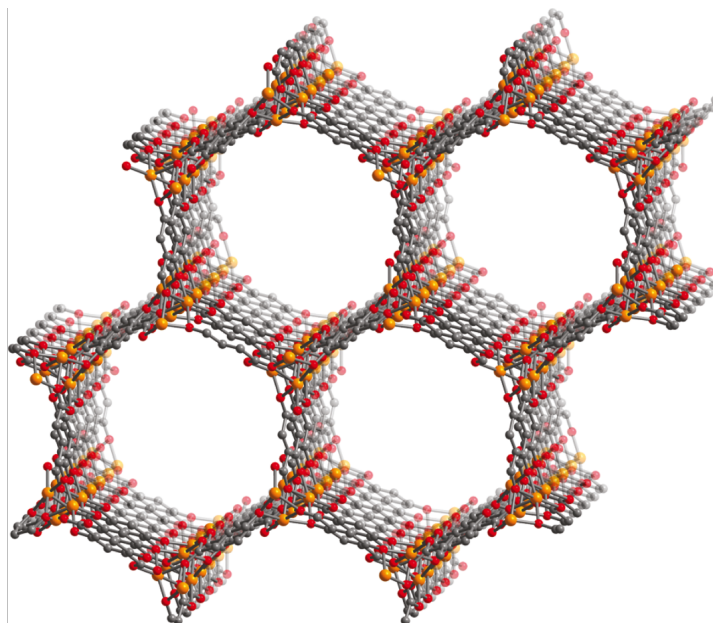


Figure 2.9: Three-dimensional molecular structure of $\text{Fe}_2(\text{dobdc})$ from powder XRD measurements. The five-coordinated $\text{Fe}(\text{II})$ active sites are lined along the hexagonal channels of the MOF. Fe: orange spheres, C: grey spheres, O: red spheres. Hydrogen atoms are omitted for clarity. Taken from 36.

determined by Brunauer-Emmett-Teller (BET) measurements. Along the channels, the coordinatively unsaturated $\text{Fe}(\text{II})$ active centers are accessible.

$\text{Fe}_2(\text{dobdc})$ is synthesized by the reaction of anhydrous FeCl_2 with 1,4-dihydroxyterephthalic acid (H_4dobdc) in dimethylformamide (DMF) and methanol at elevated temperatures (393 K) under exclusion of oxygen.³⁶ After the synthesis, residual DMF molecules are coordinated to $\text{Fe}(\text{II})$ ions, blocking the active centers of the framework. To remove the solvent, the compound is soaked in methanol for solvent exchange and evacuated in dynamic vacuum ($< 10 \text{ mbar}$) to yield $\text{Fe}_2(\text{dobdc})$ as a light green powder.

The reaction of $\text{Fe}_2(\text{dobdc})$ with different molecules, like O_2 , N_2 or NO , has been tested with regards of gas separation. In addition, a recent study showed that $\text{Fe}_2(\text{dobdc})$ is capable of oxidizing ethene to ethanol in the presence of N_2O . During the reaction, N_2O adsorbs at the $\text{Fe}(\text{II})$ centers, at which it dissociates, resulting in an $\text{Fe}(\text{III})\text{-OH}$ species and the release of molecular N_2 .

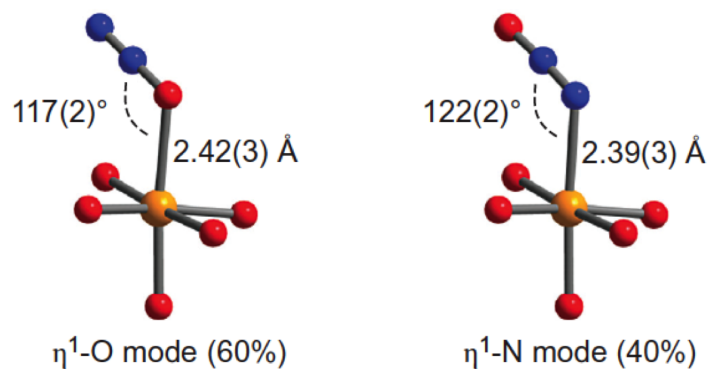


Figure 2.10: Calculated structures for adsorbed N_2O at $\text{Fe}_2(\text{dobdc})$ active sites. Fe: orange spheres, O: red spheres, N: blue spheres. Taken from 36.

2.4.3 Interaction of $\text{Fe}_2(\text{dobdc})$ with N_2O

The interaction of $\text{Fe}_2(\text{dobdc})$ with N_2O has been investigated by experimental and computational methods.⁹ To characterize the binding mode of N_2O to the Fe(II) coordination sites, powder neutron diffraction measurements have been carried out after the $\text{Fe}_2(\text{dobdc})$ sample has been exposed to various amounts of N_2O at room temperature. At low exposures, the experimental data shows two N_2O species coordinated to the active centers of the MOF with about 40 % bonded via the N-end and 60 % bonded via the O-end of the molecule. The Fe- N_2O bond length is 2.42(3) Å for the O-bonded species and 2.39(3) Å for the N-bonded species with a bond angle of about 120° in both cases (Fig. 2.10). Density functional calculations using the M06 functional are in good agreement with the experimental values. In addition, the calculations show that the coordination of N_2O via the O-end is favoured over the coordination via the N-end by 1.1 kJ/mol and, therefore, explain the 60/40 ratio of the binding modes of the two species.

After heating the sample to 60°C, the oxidation of the Fe centers by adsorbed N_2O molecules is observed. The proposed oxidation product $\text{Fe}_2(\text{OH})_2(\text{dobdc})$ has been verified by powder X-ray diffraction, however, the source of the hydrogen atom remains uncertain.

To understand these findings and get a better view on the mechanism of N_2O de-

composition, the adsorption of N_2O on $\text{Fe}_2(\text{dobdc})$ is studied in this work by the use of UHV-FTIR spectroscopy. Due to the high sensitivity towards the vibrational frequencies of adsorbed N_2O species, even small differences can be detected, which can help to determine the active species during the decomposition.

3 Experimental Section

The UHV-FTIR experiments on the $\text{TiO}_2(110)$ single crystal surface and the $\text{Fe}_2(\text{dobdc})$ powder sample were performed using a PREVAC UHV system combined with a Bruker VERTEX 80v vacuum IR spectrometer. A detailed description of the setup is given in chapter 3.1. All FTIR spectra were recorded as difference spectra averaged over 512 scans with a resolution of 4 cm^{-1} for both, transmission mode and reflection mode. Background spectra were recorded before each set of measurements.

The rutile $\text{TiO}_2(110)$ single crystal was commercially obtained (MaTeck) with a surface orientation accuracy of 0.2° . The crystal was fixed on a sample holder for measurements in reflection mode and transferred into the UHV system. The surface was prepared by repeated cycles of argon ion sputtering ($p_{\text{Ar}} = 1 \cdot 10^{-5} \text{ mbar}$, $U_{\text{sput}} = 1.4 \text{ kV}$, $I_{\text{emis}} = 10 \text{ mA}$) and annealing at 850 K in O_2 atmosphere.

$\text{Fe}_2(\text{dobdc})$ was provided by the group of J. R. Long (University of California, Berkeley) and was synthesized according to Ref. 36. The sample was pressed into the holes of a stainless steel grid ($0.5 \times 0.5 \text{ cm}^2$) under argon atmosphere and fixed onto a sample holder for transmission experiments. A specially designed transfer chamber was used to transfer the sample into the UHV chamber under exclusion of oxygen. Residual adsorbants were removed by annealing the sample at 435 K for 5 min .

O_2 (99.999 %, Westfalen AG) and Ar (99.999 %, Westfalen AG) for preparation and N_2O (99.5 %, Air Liquide), CO (99.999 %, Westfalen AG) and N_2 (99.999 %, Westfalen AG) for adsorption experiments were commercially obtained and used without further purification.

3.1 The FTIR-UHV System

The FTIR-UHV system contains two major parts - a UHV system (PREVAC) and a vacuum FTIR spectrometer (Bruker, VERTEX 80v) connected to each other. A specially designed sample manipulator enables the acquisition of reflection-absorption IR spectra at grazing incidence on single crystal surfaces as well as the measurement of FTIR

transmission spectra of powder samples. Furthermore, the entire optical path of the IR beam is evacuated to remove background signals of atmospheric gases, like CO, CO₂ or H₂O. As a prototype of novel UHV-FTIR systems, this setup allows the acquisition of high-quality and high sensitivity FTIR spectra for the characterization of adsorbate species on single crystal surfaces and powder samples. A schematical overview of the system is shown in Figure 3.1.

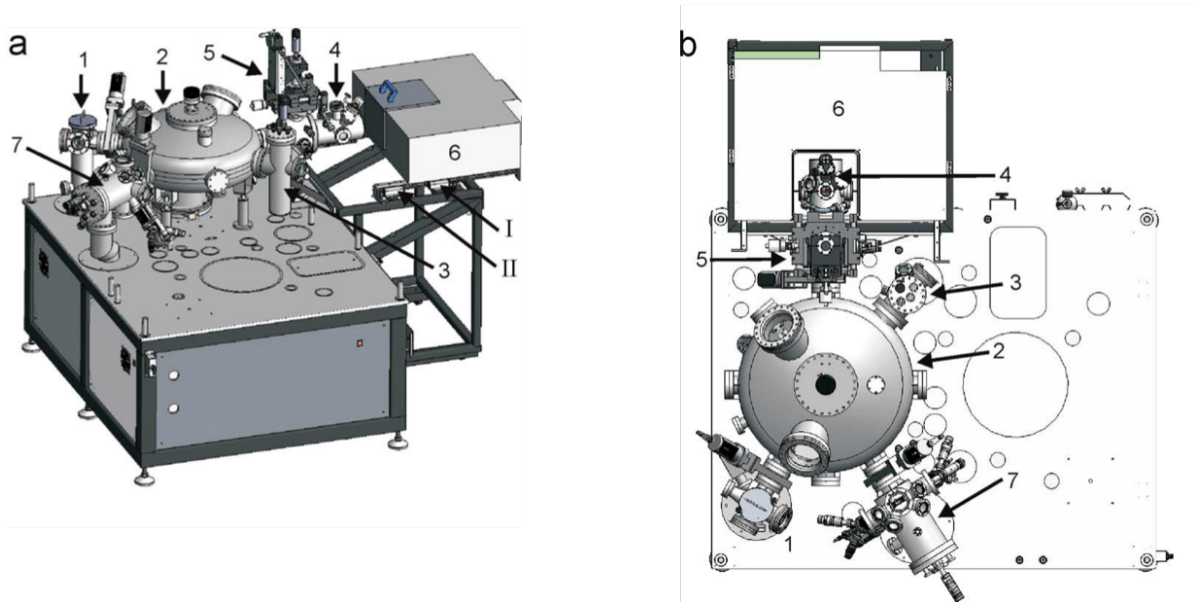


Figure 3.1: Schematical setup of the UHV-FTIR system in (a) perspective side view and (b) top view with load-lock (1), distribution (2), magazine (3) and measurement chambers (4), sample manipulator (5), UHV-FTIR spectrometer (6) and preparation chamber (7).⁴¹

The core of the system is the distribution chamber, from which five smaller UHV chambers with different purposes are accessible - namely the load-lock, preparation, magazine, high pressure and measurement chambers. The chambers are separated from the distribution chamber by gate valves. A special, circular transfer mechanism based on a rotary feedthrough at the distribution chamber is used to transfer the sample holder within the chambers. The UHV conditions in the distribution chamber are maintained by the use of an ion getter pump (IGP) and a titanium sublimation pump (TSP) yielding a base pressure of $1 \cdot 10^{-10}$ mbar after bake-out. The load-lock chamber is pumped by

a turbomolecular pump (TMP) and a rotary vane pump, achieving a base pressure of $<1 \cdot 10^{-6}$ mbar within a few minutes after venting the chamber with gaseous N_2 . This allows a quick transfer of a sample from atmospheric conditions into the UHV system without disturbing the vacuum inside the other chambers. The preparation chamber is used to prepare the sample under UHV conditions without affecting the vacuum inside the other chambers by sample cleaning or dosing of organic molecules. The chamber is equipped with a TMP and a rotary vane pump to give a base pressure of $1 \cdot 10^{-9}$ mbar. A newly installed high pressure chamber (not shown in Fig. 3.1) allows the preparation of powdered catalyst samples at ambient pressure and even higher pressures up to 20bar. For that, a dedicated high pressure cell can be pressed to the sample holder separating the sample from the rest of the chamber. This system allows to expose the sample to different gases with a pressure of up to 20 bar to simulate real catalytic conditions. In addition, electrical and thermal contacts enable sample temperatures from 200 K to 600 K. A TMP combined with a rotary vane pump is used to evacuate the high pressure chamber for the sample transfer. The distribution chamber is also equipped with a magazine chamber, which features six stations for sample holders to store samples under UHV conditions. Within the magazine chamber, a manipulator moves the single stations up- and downwards to switch between the samples.

The measurement chamber is specially designed for UHV-FTIR measurements in transmission and reflection mode. This chamber is pumped by a TMP and a diaphragm pump to yield pressures below $1 \cdot 10^{-10}$ mbar and is additionally equipped with an ion source for sputtering and two dosing valves for adsorption experiments. A manipulator system allows to translate the sample inside the chamber along the x-, y-, and z-axis, as well as to rotate the sample about the x-axis. The sample holder station is equipped with pneumatically controlled heating and cooling contacts and a thermocouple (K type) for temperature control. At a pressure of 3 bar, the electrical contacts are pressed against the sample holder, allowing to heat the sample *via* electron beam heating (for single crystals) or resistive heating (for powder samples). At a pressure of >5 bar, a sapphire ball is pressed against the cooling contact of the sample holder. A liquid nitrogen flow-

through cooling line provides sample temperatures as low as 100 K. Figure 3.2 shows the sample holder (PREVAC, PTS-H/K 1000) for transmission FTIR measurements. The sample itself is pressed INTO a small metal grid and fixed on top of the sample holder. For single crystal measurements, another sample holder (PREVAC, PTS-EB 1200) is used. The single crystal is fixed on a tantalum plate by tantalum sheets that are placed in the notch of the crystal and fixed at the sample holder to ensure good thermal contact of the sample.

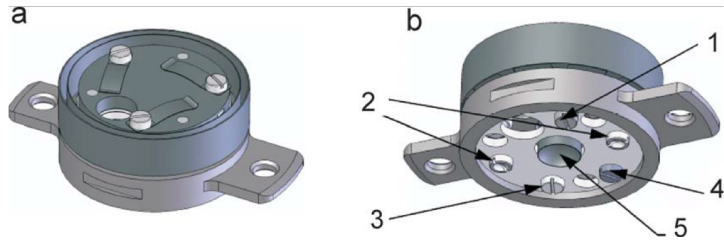


Figure 3.2: Schematical setup of the sample holder (PREVAC, PTS-H/K 1000) for transmission measurements in (a) top view and (b) bottom view with different contacts: 1) potential, 2) heating, 3) Ni thermocouple, 4) NiCr thermocouple, 5) cooling.⁴¹

The Bruker VERTEX 80v vacuum FTIR spectrometer is connected to the measurement chamber with two KBr windows on each side of the incident and emergent beam path. The space between the windows is sealed by a specially designed connector system, which can be evacuated to give a pressure of $<1 \cdot 10^{-5}$ mbar preventing the absorption of IR radiation by residual gas molecules in the beam path. Furthermore, the FTIR spectrometer is evacuated by a multi-stage roots pump, which results in a fully evacuated IR beam path (see Fig. 3.3). The actively aligned UltraScan[®] interferometer with an optical resolution of 0.2 cm^{-2} and integrated dual-channel 24-bit analog-to-digital(A/D) signal converters provide high-quality data acquisition with low signal-to-noise ratios, thus allowing even the detection of weak absorption signals.

To enable measurements in transmission and reflection mode, the spectrometer is equipped with 2 different detectors: For measurements in transmission mode, a deuterated triglycine sulfate (DTGS) detector is used, while a liquid nitrogen cooled mercury-cadmium-telluride (MCT) detector is required for the reflection-absorption IR (RAIRS)

measurements. To change between transmission mode and reflection mode, the spectrometer is vented and a mirror inside the spectrometer is slightly tilted to focus the IR beam on the single crystal surface at an angle of 80° with respect to the surface normal.

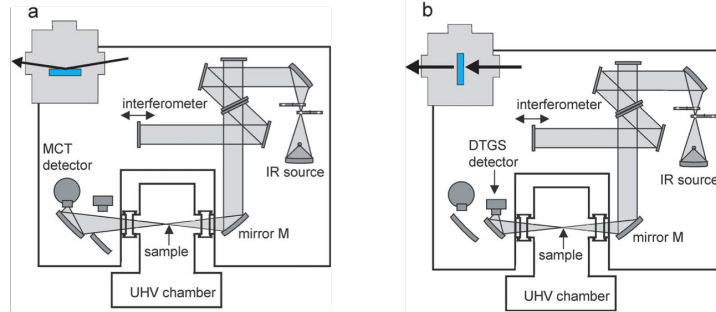


Figure 3.3: Schematic setup of the IR beam path for (a) reflection-absorption and (b) for transmission IR measurements.⁴¹

3.2 Sample Preparation

UHV-FTIR measurements require clean sample surfaces in order to achieve reasonable and reproducible results. After storage under atmospheric conditions, both, powder samples and single crystals, show high amounts of contaminants - such as H_2O , O_2 , CO or CO_2 - adsorbed on the surface of the samples. This section describes the processes used for sample preparation prior to UHV-FTIR experiments.

3.2.1 Preparation of a $\text{TiO}_2(110)$ Single Crystal

The rutile $\text{TiO}_2(110)$ single crystal is fixed on a sample holder for single crystals (PRE-VAC, PTS-EB 1200) and transferred into the UHV system.

In order to remove contaminants from the surface of the rutile $\text{TiO}_2(110)$ single crystal, the sample is sputtered with Ar^+ ions at room temperature. For that, the measurement chamber is filled with argon gas up to a pressure of $1 \cdot 10^{-5}$ mbar. The argon atoms are ionized by an ion source consisting of an anode and a cathode, to which a high voltage of 1.4 kV is applied. The electrostatic field creates a plasma, which is accelerated towards the surface of the sample that is held at negative potential. The impact energy of the

Ar⁺ ions is transferred to surface atoms and adsorbate species causing them to desorb from the surface.

After sputtering, the crystallinity of the surface is disturbed due to missing surface atoms or argon ions implemented in the crystal lattice of the sample. To restore the well-ordered structure of the surface, the sample is heated to elevated temperatures under UHV conditions. The thermal energy excites lattice vibrations in the crystal that cause the reorganisation of the surface structure. At the same time, contaminants from the bulk diffuse to the surface and can be removed by ion sputtering. The process of repeated sputter anneal cycles enables the preparation of a smooth, well-ordered surface.

However, the amount of oxygen vacancies at the surface is rather high after the preparation and needs to be diminished in order to get reproducible results. Accordingly, the last sputter anneal cycle before every experiment involves heating the sample to 850 K in oxygen atmosphere ($p_{O_2} = 1 \cdot 10^{-6}$ mbar), which gives an oxidized sample surface with only a small amount of oxygen vacancies.²⁴

3.2.2 Preparation of a Fe₂(dobdc) Powder Sample

Fe₂(dobdc) was provided by the group of J. R. Long (University of California, Berkeley) and synthesized according to the literature.³⁶ The yellow-greenish powder sample was stored under inert gas atmosphere to avoid the adsorption of atmospheric gas species like H₂O or CO₂. In a glove box, the sample is applied to a stainless steel grid and mechanically pressed to give a thin but stable sample for transmission FTIR measurements. The grid is mounted on a sample holder (PREVAC, PTS-H/K 1000) for transmission experiments and transferred to a specially designed transfer chamber, which allows to bring the sample inside the UHV system under exclusion of oxygen.

To remove adsorbed species inside the framework, the sample is annealed at 435 K for 5 min under UHV conditions. Afterwards, the sample is cooled to 100 K with liquid nitrogen for the adsorption of CO and N₂O.

3.3 Adsorption Experiments

The adsorption of molecules on the different sample surfaces is achieved using a gas dosing system attached to the measurement chamber. The system contains three separate capillary lines with pressure reducing valves for small gas containers as well a glass-metal transition for liquid adsorbate species. Leak valves between the measurement chamber and the gaslines enable a controlled dosing of the molecules to the chamber.

The gaslines are continuously pumped by a combination of a TMP and a diaphragm pump (Pfeiffer HiPace) to remove contaminants from the capillaries and ensure a high purity of the dosed gases. The base pressure inside the gas dosing system is $<1 \cdot 10^{-6}$ mbar. To ensure a high purity of the dosed molecules, the line is repeatedly filled with the desired gas and pumped until the base pressure is reached again before dosing, since the attachment of the gas bottles to the pressure reducer can cause further impurities in the gasline.

For the adsorption experiments, the gasline is closed towards the pump side and filled with the desired gas. The leak valve at the chamber side is opened and the pressure is adjusted to a certain value for a fixed amount of time. To quantify the dose of the provided gas molecules, a commonly used unit in surface science is the langmuir [L]. Historically, one Langmuir corresponds to a pressure of $1 \cdot 10^{-6}$ torr for a time of 1 second, and is roughly the amount that covers a surface with one monolayer of the adsorbate. Converting this to the more commonly used millibar gives

$$1L = 1,33 \cdot 10^{-6} \text{ mbar} \cdot \text{s}. \quad (7)$$

However, using Langmuir to determine the surface coverage with an adsorbate is only applicable under following assumptions: 1) The surface contains a single type of adsorption site. 2) The adsorption sites are not influenced by each other. 3) Every adsorbed molecule stays at the adsorption site and does not desorb during the process. In the case of TiO_2 these assumptions are not fulfilled, because of the heterogeneous structure of the rutile $\text{TiO}_2(110)$ surface. The $\text{TiO}_2(110)$ surface consists of alternating rows of

Ti and O atoms, from which every second row of Ti atoms is covered by bridging O atoms. This leaves only 1/4 of surface atoms, that can act as active adsorption centers and, therefore, a dosage of less than 1 L is sufficient to saturate the surface.

The unit Langmuir is used mostly as a dosage for single crystal surfaces. Adsorption measurements on powder samples, as for example nanoparticles or MOFs, require much larger dosages to saturate the large surface area of the samples and the use of Langmuir is no longer reasonable. In addition, the transmission IR spectra are measured *in situ* during the exposure to the adsorbate and the dosage of the adsorbate cannot be determined exactly. Therefore, only the time and the pressure during dosing are given to quantify the dosage for powder measurements.

3.4 UV-light Induced Photoreaction

UV irradiation of the TiO₂(110) sample was performed *in situ* during a series of repeated FTIR measurements after the sample has been exposed to the adsorbate. For that, a UV-LED source (Spectroline, OPTIMAX 365) with a wavelength of 365 nm and a maximum intensity of 50 mW/cm² was fixed at a window on top of the measurement chamber. The incident light beam irradiated the surface at an angle of 0° to the surface normal. The electrical intensity stabilizer of the UV source assures a constant intensity directly after turning on the device. Other light sources, such as windows in the UHV chamber, were covered with tin foil. The comparison of the measured spectra gives a time-resolved progress of the adsorbates' vibrational frequencies during UV irradiation.

4 Results and Discussion

The results of the UHV-FTIR studies on a rutile $\text{TiO}_2(110)$ single crystal surface and a $\text{Fe}_2(\text{dobdc})$ powder sample are shown in this section. The samples were prepared and cooled to different temperatures in the range of 90 K to 150 K and exposed to various amounts of N_2O . Before every set of measurements, a background spectrum was recorded that was subtracted from the measured spectra to give the IR signals of the adsorbed species. The thermal desorption of the adsorbed molecules was examined by heating the sample and subsequent cooling to the initial temperature to ensure the same conditions during the single FTIR measurements. The photoreaction of N_2O adsorbed on the $\text{TiO}_2(110)$ single crystal surface was investigated by irradiation of the sample with UV light with a wavelength of 365 nm. *In situ* performed IR measurements during the irradiation give a time-resolved progress of the photoinduced depletion of the absorption signals. To characterize the adsorption sites of the $\text{Fe}_2(\text{dobdc})$ powder sample, the sample was exposed to different amounts of CO. The high-intensity signal of CO is used to distinguish between the single adsorption sites on the sample surface. Afterwards, the clean sample was exposed to N_2O and the thermal desorption of the adsorbate was studied.

4.1 Reflection-Absorption IR Experiments

4.1.1 N_2O Adsorption on $\text{TiO}_2(110)$

After preparation, the clean rutile $\text{TiO}_2(110)$ sample was cooled down to 102 K, 108 K, 117 K, and 148 K, respectively, and exposed to N_2O . The UHV-FTIR spectra were measured in absorption-reflection geometry at grazing incidence with an angle of 80° with reference to the surface normal.

Figure 4.1 shows the IR spectra of the rutile $\text{TiO}_2(110)$ single crystal exposed to various amounts of N_2O at 102 K. Spectrum A shows no absorption signals and corresponds to the clean sample surface after preparation. After exposure to 0.25 L N_2O (spectrum B), two absorption signals appear at 2241.1 cm^{-1} and 1234.2 cm^{-1} . The signals can be

assigned to the asymmetric and symmetric stretching modes of N_2O .

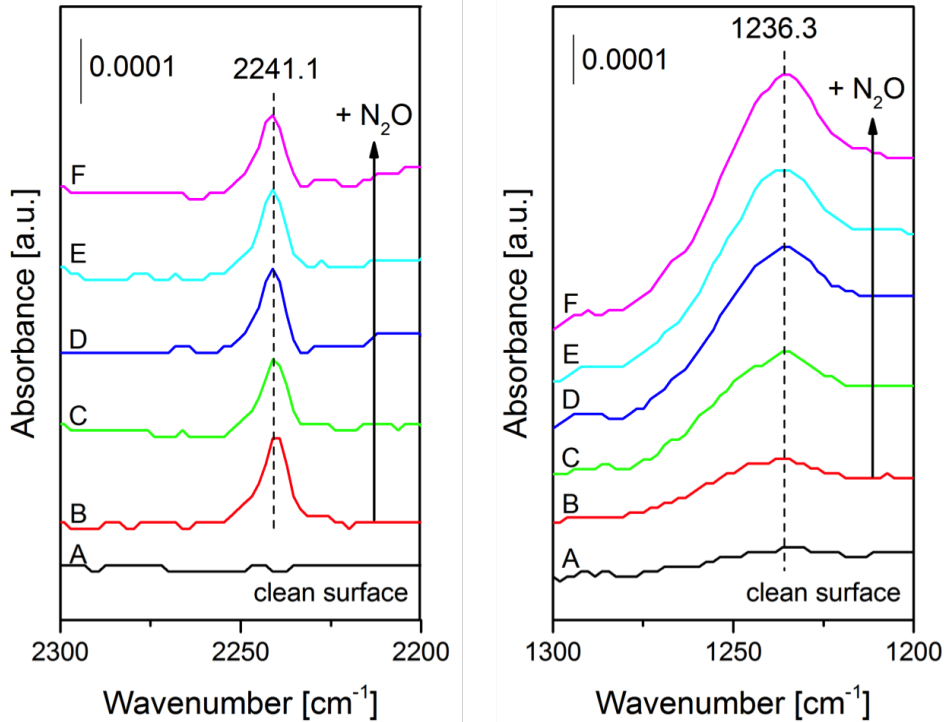


Figure 4.1: UHV-FTIR spectra of the α - $TiO_2(110)$ single crystal surface at 102 K after exposure to different amounts of N_2O . (A) Clean surface, (B) 0.25 L N_2O , (C) 1.25 L N_2O , (D) 2.25 L N_2O , (E) 4.25 L N_2O , (F) 10.25 L N_2O .

The asymmetric stretching mode at 2241.1 cm^{-1} can be described as a nitrogen-nitrogen stretching motion $\nu_{NN}(N_2O)$, while the symmetric stretch corresponds to the nitrogen-oxygen stretching motion $\nu_{NO}(N_2O)$ of the adsorbate. The signal for the asymmetric stretching mode is blueshifted, while the symmetric stretching mode is redshifted with regards to the gas phase IR spectrum of N_2O , which shows two signals at 2224 cm^{-1} and 1285 cm^{-1} .²⁰ The signal shift of the adsorbed N_2O can be explained considering its resonance structures (see Fig. 2.4). The O-bonded species at the active site should stabilize structure A leading to a decrease in the force constant of the N-O bond. Therefore, the N-O stretching mode of adsorbed N_2O is shifted towards higher wavenumbers, whereas the increase of the N-N force constant causes a redshift of the asymmetric N-N stretching mode.

Interestingly, the intensity of the $\nu_{NN}(N_2O)$ stretching mode does not increase with increasing amount of dosed N_2O . Therefore, it can be assumed that the surface is already saturated after exposure to 0.25 L N_2O . An explanation for this can be given considering that the theory after which 1 L corresponds to 1 monolayer of adsorbed species is based on the simplified Langmuir adsorption mechanism. N_2O only binds to Ti sites at the surface. Since the surface consists of both, oxygen and titanium atoms, the amount of active sites on the surface is smaller, than the amount of total atoms on the whole surface area. Thus, the amount of N_2O to cover the surface with one monolayer is smaller than 1 L. However, the intensity of the $\nu_{NO}(N_2O)$ stretching mode at 1234.2 cm^{-1} increases with higher amounts of dosed N_2O . Therefore, a control measurement of the clean surface (not shown) has been carried out to determine the source of the increasing signals in the area from 1500 cm^{-1} and 500 cm^{-1} . During the time of 1 *h*, several spectra were recorded that also showed a shift in the background in this region. A possible explanation for this are minor temperature changes at the sample, which cause the background to differ from the original background recorded prior to the experiment. Since the region of the $\nu_{NN}(N_2O)$ stretching mode is not affected by these changes, the quantitative analysis of the thermal and catalytical N_2O depletion on the sample surface is carried out using the $\nu_{NN}(N_2O)$ stretching mode signal.

Figure 4.2 shows the UHV-FTIR spectra of the rutile $TiO_2(110)$ surface after saturation with N_2O at different temperatures. At higher temperatures, namely 108 K and 117 K, no additional signals appear in the IR spectra, and still only the vibrational modes of O-bonded N_2O species can be found at about 2240 cm^{-1} . At 148 K no N_2O adsorption has been observed by UHV-FTIR measurements, which is in good agreement with a desorption temperature of 130 K determined by TPD measurements of adsorbed N_2O at rutile $TiO_2(110)$ single crystals.⁶ The TPD measurements of Henderson et al. also showed another peak at 170 K, which has been assigned to N_2O desorbing from oxygen vacancies on a (partially) reduced $TiO_2(110)$ surface.

In contrast to previous experimental studies^{6,20} and DFT calculations³³ of N_2O adsorption on TiO_2 , the experiments in this work only show one pair of correlated vibra-

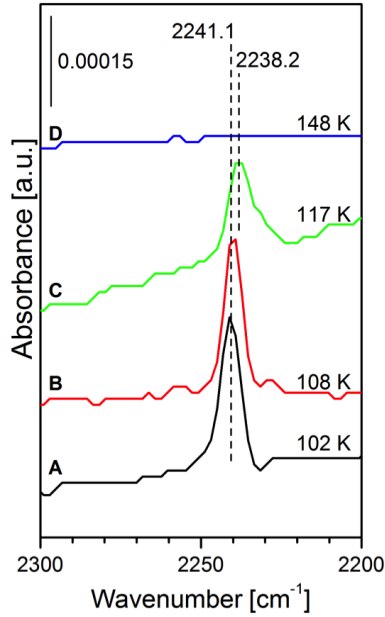


Figure 4.2: UHV-FTIR spectra of the α -TiO₂(110) single crystal surface after exposure to N₂O at (A) 102 K, (B) 108 K, (C) 117 K and (D) 148 K.

tional signals in the IR spectra, indicating a single adsorption geometry of N₂O on the oxidized rutile TiO₂(110) surface. Rusu et al.²⁰ observed two sets of correlated stretching modes on TiO₂ nanoparticles at 2262/1313 cm^{-1} for the N-bonded species and at 2237/1251 cm^{-1} for the O-bonded species, respectively. Another set of correlated signals has been observed during thermal desorption of the adsorbate at 2245/1234 cm^{-1} , which is assigned to the O-bonded N₂O species at minority active sites. DFT calculations on the adsorption of N₂O proposed two possible adsorption geometries as well, either via the N-atom (N_{ad}) or via the O-atom (O_{ad}). The calculated vibrational frequencies for the equilibrium structures of both species are at 2298/1366 cm^{-1} for the N-bonded configuration and at 2250/1227 cm^{-1} for the O-bonded configuration, whereas the intensity of the $\nu_{NO}(N_2O)$ stretching mode is only about 1 % of the $\nu_{NO}(N_2O)$ stretching mode. The adsorption energies of both structures ($E_{ad} = -29.8 kJ \cdot mol^{-1}$ for O_{ad} and $-32.8 kJ \cdot mol^{-1}$ for N_{ad}) differ by 3.0 $kJ \cdot mol^{-1}$ and, therefore, the structures are considered to be similar in energy.³³ However, in another experimental study, the formation of N₂O from adsorbed NO at a TiO₂(110) surface only gives one signal for the adsorbed

N_2O in UHV-FTIR measurements at 2243 cm^{-1} , denoted as the $\nu_{NN}(\text{N}_2\text{O})$ stretching mode.⁴²

Comparing the results from literature with the results shown in Figure 4.1 gives slight deviations of the position of the $\nu_{NN}(\text{N}_2\text{O})$ stretching mode of adsorbed N_2O on the single crystalline $\text{TiO}_2(110)$ surface. Due to the spectral resolution of 4 cm^{-1} , it is also possible that the signal at 2241 cm^{-1} is not fully resolved and indicates a combination of the overlapped signals corresponding to the $\nu_{NN}(\text{N}_2\text{O})$ stretching mode of Ti-ONN and Ti^* -ONN proposed by Rusu et al. However, the only signal corresponding to the $\nu_{NO}(\text{N}_2\text{O})$ stretching mode appears at 1234 cm^{-1} , indicating the presence of an O-bonded N_2O species at minority sites, like for example bridging oxygen vacancies. In order to get more information on the adsorption mechanism, the thermal desorption of N_2O was examined by another set of UHV-FTIR measurements.

4.1.2 Thermal Desorption of N_2O

Thermal desorption of N_2O was studied by heating the $\text{TiO}_2(110)$ single crystal to a certain temperature and subsequent cooling of the sample to the initial temperature. Thus, the same experimental conditions during all measurements are ensured and deviations from the previously recorded background spectrum are minimized. For the quantification of the desorption reaction, the observed $\nu_{NN}(\text{N}_2\text{O})$ signals in the IR spectra were fitted by a gaussian function and the peak area was calculated for the single measurements. The relative peak area has been calculated with regards to the initial peak area before heating. By plotting the relative peak area against the corresponding temperature during heating, a temperature-resolved desorption curve of the process is obtained.

The IR spectra after each heating step (Fig. 4.3a) show a decrease in intensity of the $\nu_{NN}(\text{N}_2\text{O})$ stretching mode caused by the thermal desorption of N_2O . The desorption rate based on the decreasing relative peak areas of the $\nu_{NN}(\text{N}_2\text{O})$ stretching vibration (Fig. 4.3b) shows a total desorption of N_2O from the surface at around 130-140 K.

The results are in good agreement with TPD measurements of Henderson et al.⁶ and

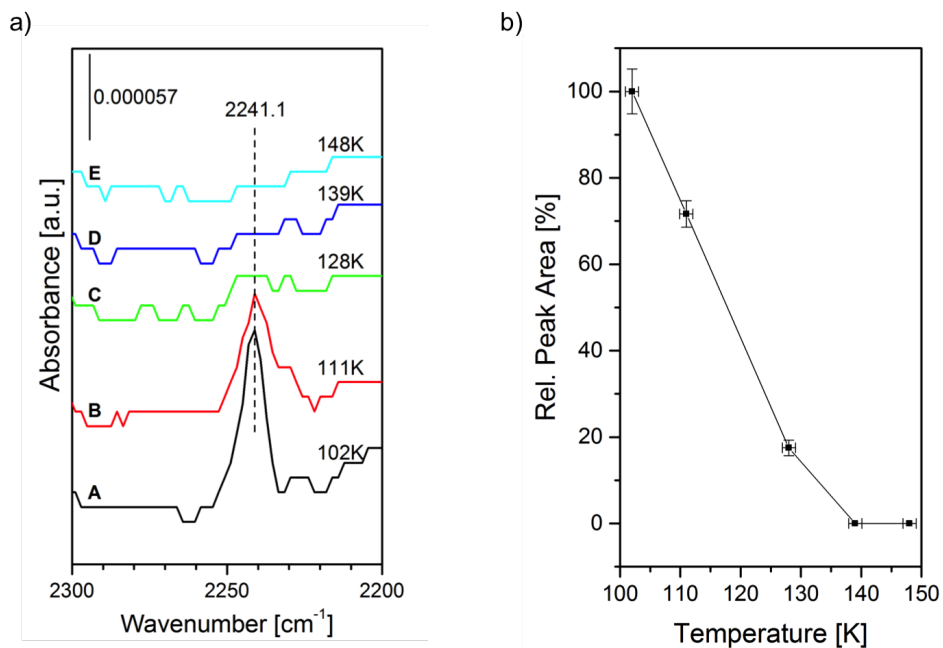


Figure 4.3: UHV-FTIR spectra of the α -TiO₂(110) single crystal surface at (A) 102 K, (B) 111 K, (C) 128 K, (D) 139 K and (E) 148 K during annealing.

Kim et al.⁴³, who observed a N₂O desorption temperature of 130-145 K depending on the coverage of the TiO₂(110) surface for N₂O adsorbed at Ti⁴⁺ sites. A second peak in the TPD measurements at around 170 K was assigned to N₂O adsorbed at oxygen vacancy sites. This species is not observed during the thermal desorption of N₂O in this work, indicating a totally oxidized TiO₂(110) surface. However, it is reported that even after oxidizing the surface during preparation, the amount of oxygen vacancies on the surface is still around 3-5 %.²⁴ Due to the low intensity of the obtained signals, it is possible that the amount of oxygen vacancy adsorbed N₂O is too small and, therefore, the presence of this species is not detectable by IR measurements.

4.1.3 Photoreaction of N₂O on TiO₂(110)

The photoreaction of adsorbed N₂O on the oxidized TiO₂(110) surface has been investigated by time-resolved UHV-FTIR spectroscopy at 102, 108 and 117 K. For that, the sample has been cooled to the desired temperature and exposed to N₂O until the surface was saturated. Afterwards, several IR spectra were recorded *in situ* during the irradi-

ation of the sample by an UV light source ($\lambda = 365 \text{ nm}$). To obtain a time-resolved progress of the N_2O depletion, the signal for the asymmetric $\nu_{NN}(\text{N}_2\text{O})$ stretching mode has been fitted by a gaussian function for every spectrum and the area of the signal has been determined. The relative peak area is calculated with regards to the initial peak area, and plotted against the irradiation time to give a time-dependent N_2O depletion diagram.

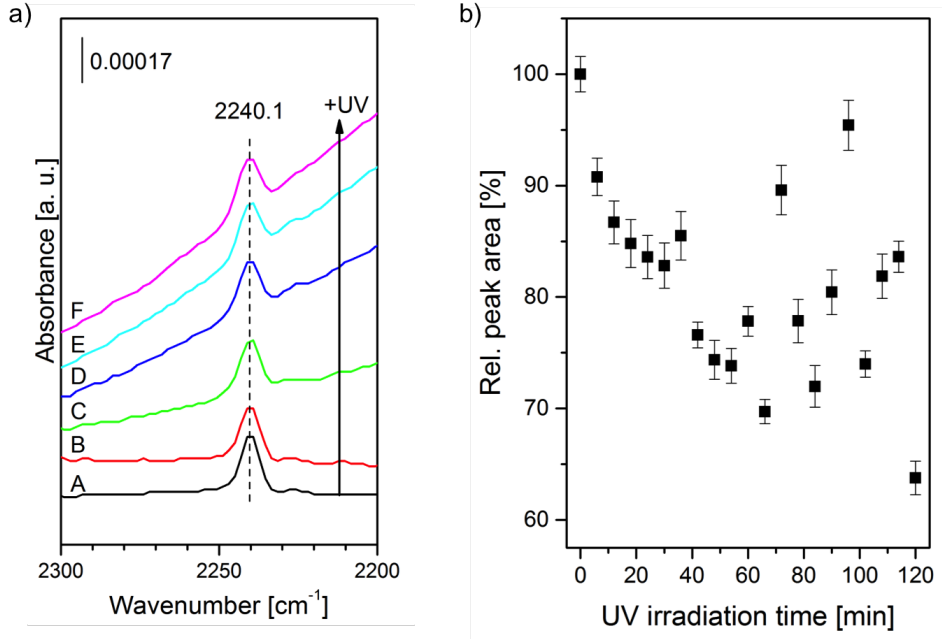


Figure 4.4: left: UHV-FTIR spectra of the $\alpha\text{-TiO}_2(110)$ single crystal surface exposed to N_2O at 102 K during UV irradiation. (A) 0 min UV, (B) 30 min UV, (C) 60 min UV, (D) 90 min UV and (E) 120 min UV. right: Time-dependent N_2O depletion during UV irradiation at 102 K.

Figure 4.4a shows the IR spectra of the N_2O saturated rutile $\text{TiO}_2(110)$ surface at 101 K after different UV irradiation times. During irradiation, the signal at 2241 cm^{-1} assigned to the $\nu_{NN}(\text{N}_2\text{O})$ stretching mode decreases, indicating the depletion of adsorbed N_2O at the surface. No additional signals appear in the whole measurement range. After about 60 min the IR spectra seem tilted due to an increase in intensity of the background. The time-dependent depletion of N_2O during UV irradiation is shown in Figure 4.4b. During the first 60 min, the relative peak area of the $\nu_{NN}(\text{N}_2\text{O})$ stretching mode signal decreases to about 75 % of the initial signal area. After that time,

the signals spread randomly around 72 % and 96 %, and a correlation between UV irradiation time and the corresponding signal depletion of adsorbed N_2O is not longer observed. The large spread of this values could arise from readsorbed N_2O at the surface. However, due to the low pressure of $1 \cdot 10^{-10}$ mbar inside the measurement chamber during data acquisition and the random distribution of the data points, this possibility is not likely. Another possibility for the random distribution after longer irradiation time is the observed shift in the background of the IR spectra (see Fig. 4.4a). The resulting asymmetric signals are no longer suitable to be fitted by a gaussian function and, therefore, a significant analysis of the depletion curve after an irradiation time of 60 min is not possible. Nevertheless, the decrease of the signal during UV irradiation within the first 60 min of the experiment is assigned to photoinduced processes on the surface causing the depletion of adsorbed N_2O at the surface. The possible reactions are discussed further below.

To investigate the influence of reaction temperature, the photoreaction experiments have been carried out at 102, 108 and 117 K. The time-dependent depletion diagrams at the three different temperatures are shown in Figure 4.5.

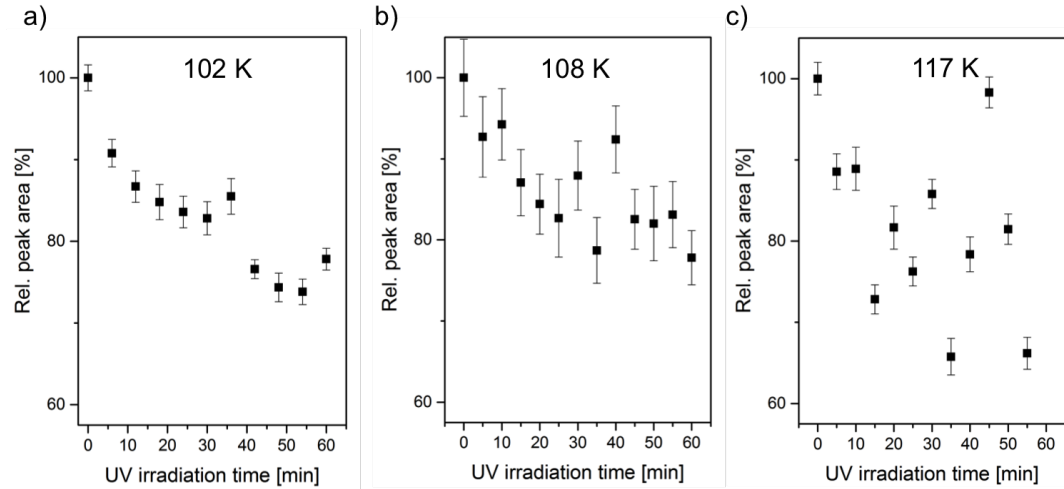


Figure 4.5: Time-dependent N_2O depletion diagrams during UV irradiation at a) 102 K, b) 108 K and c) 117 K.

At 102 K (Fig. 4.5a), the graph shows a decrease of the $\nu_{NN}(N_2O)$ stretching mode peak area of about 25 % with regard to the initial peak area after N_2O dosing. Fitting

the data points by linear or exponential decay fitting functions has not given reasonable results due to the large spread of the data points. However, two different regions are apparent in the graph. In the first 10 min, the diagram shows a fast decrease of 15 % which is followed by a slower decrease rate during the last 50 min of the experiment. After about 60 min, a shift in the background distorted the detected signals and the analysis gave no reasonable results (see Fig. 4.4a). The shift occurred at all measurements on the $\text{TiO}_2(110)$ single crystal surface and is assumed to be caused by slight temperature variations during the experiment altering the background spectrum recorded prior to UV irradiation. Therefore, a progress for longer UV irradiation times could not be investigated.

The depletion diagram at 108 K (Fig. 4.5b) shows a similar progress for the N_2O depletion with a decrease of the $\nu_{NN}(\text{N}_2\text{O})$ stretching mode signal of about 20 % after 60 min. However, a significant correlation between irradiation time and N_2O depletion could not be shown due to the large error of up to ± 5 % for the single peak area calculations. This large error is caused by irregular peak shapes, which differ from the usual gaussian peak shape in IR spectra. Pressure fluctuations in the IR beam path, which lead to slight differences in the detected absorbance and, with that, to irregular peak shapes are a possible reason for the error. Especially for low intensity signals, these fluctuations have a large impact on the signal shapes and affect the quantification of these signals essentially.

Figure 4.5c shows the N_2O depletion diagram at 117 K. The data points are randomly distributed in a range of 65 to 100 % and a correlation between UV irradiation time and the depletion of the $\nu_{NN}(\text{N}_2\text{O})$ stretching mode signal is not verifiable based on these results.

In all three measurements, it is noticeable that the quantification of the depletion process during UV irradiation is limited by different factors. The most important factor is the low intensity of the observed signals in the IR spectra. Even small changes in the measured intensities bring about large relative changes when compared to each other. These small changes can also occur due to pressure fluctuations in the IR beam path,

and a differentiation between a real signal change and random errors is not possible. Furthermore, the fitting procedure only gives reasonable values for symmetric gaussian absorption signals. Deviations from the symmetric peak shape falsify the calculated values and a precise analysis of the peaks is not possible.

To understand the depletion of the N_2O signal, the possible reactions during UV irradiation have to be considered. Two different photoinduced reactions are possible: 1) The adsorbed N_2O is dissociated in a photocatalytic reaction at the surface to give molecular nitrogen and an oxygen atom adsorbed at the surface or 2) the adsorbed N_2O desorbs from the surface without decomposition. The mechanisms of both possibilities are discussed in the following.

The photocatalytic decomposition of N_2O at rutile TiO_2 is driven by the generation of electrons on the TiO_2 surface caused by UV irradiation. When the energy of the incident photons is equal to or higher than the energy of the band gap, electrons (e^-) are excited from the valence band to the conduction band of the semiconductor leaving a hole (h^+) in the valence band. The adsorbed N_2O acts as an electron scavenger and is reduced to N_2O^- followed by the dissociation into N_2 and an O^- anion adsorbed at the surface. The photocatalytic desorption is also believed to be activated by electrons generated by UV irradiation causing a charge separation in the semiconductor surface. The electron is trapped by adsorbed N_2O , but instead of dissociating into N_2 and O^- , the N_2O^- species recombines with the generated hole and the neutral N_2O desorbs from the surface.²⁰ In both cases, the reaction is driven by the generation of electrons and holes at surface near sites and a distinction between this two processes is not possible by IR measurements alone, since they both result in a decrease of the N_2O stretching mode signal.

A possibility to verify the occurring reaction is to combine UHV-FTIR spectroscopy with the simultaneous analysis of the residual gas in the measurement chamber by mass spectrometry. Due to problems with the mass spectrometer situated at the measurement chamber, this experiment have not been carried out during this work. Determining the reaction products during the irradiation time can help, to distinguish between photoin-

duced desorption, which gives only N_2O as a product, or photoinduced N_2O dissociation with gaseous N_2 as occurring reaction product.

4.2 Transmission UHV-FTIR Experiments

4.2.1 Probing the Adsorption Sites of $\text{Fe}_2(\text{dobdc})$ with CO

In order to determine the possible adsorption sites of the $\text{Fe}_2(\text{dobdc})$ framework, the sample has been cooled to 96 K and exposed to various amounts of carbon monoxide after preparation. Since CO is easily detectable in IR measurements and binds strongly to metal atoms, it is an excellent probe molecule for this occasion.⁴⁴ The obtained spectra during exposure to different amounts of CO are shown in Figure 4.6.

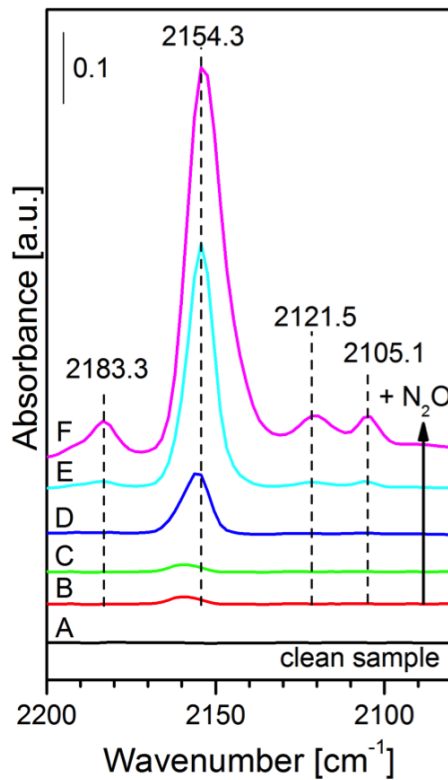


Figure 4.6: UHV-FTIR spectra of the $\text{Fe}_2(\text{dobdc})$ powder sample at 95 K during exposure to CO: (A) Clean surface, (B) $1 \cdot 10^{-6}$ mbar CO for 7 min, (C) $1 \cdot 10^{-5}$ mbar CO for 7 min, (D) $1 \cdot 10^{-5}$ mbar CO for 7 min, (E) $1 \cdot 10^{-4}$ mbar CO for 7 min and (F) $1 \cdot 10^{-3}$ mbar CO for 7 min.

Spectrum A shows no adsorption signals and corresponds to the clean $\text{Fe}_2(\text{dobdc})$

powder sample. At low CO coverage ($1 \cdot 10^{-6}$ mbar CO for 7 min, spectrum B), a single absorption band appears at 2158 cm^{-1} and is assigned to the C-O stretching vibration of adsorbed CO on the active Fe(II) centres. The signal is blueshifted by 15 cm^{-1} with regard to the gas phase ($\nu_{CO} = 2143 \text{ cm}^{-1}$). At higher coverages ($1 \cdot 10^{-6}$ mbar - $1 \cdot 10^{-3}$ mbar CO for 7 min) three additional signals appear at 2105, 2120, and 2183 cm^{-1} . The main peak is redshifted by 4 cm^{-1} to 2154 cm^{-1} . During annealing (not shown), the minor peaks disappear at 113 K, whereas the main signal decreases during the process and totally disappears at 131 K. The additional signals are assigned to minority active sites and show low absorption intensities. The appearance of different signals can be explained with structural defects in the framework of $\text{Fe}_2(\text{dobdc})$, that alter the surroundings of the active sites. Another possibility is the adsorption in a bridging geometry at the terminal Fe centers of the MOF, as it has been shown for CO_2 adsorption on the mesoporous metal-organic framework MIL-100(Fe) (MIL: Material from Institut Lavoisier).³⁷ However, it is not possible to exactly determine the origin of the minor peaks only by the shift of the signal and other techniques must be applied to analyze the chemical composition of these minority active sites.

4.2.2 N_2O Adsorption on $\text{Fe}_2(\text{dobdc})$

After determining the active sites of the $\text{Fe}_2(\text{dobdc})$ powder sample, the sample is cleaned by heating to 440 K for 30 min and cooled to 95 K for the adsorption of N_2O . During exposure, *in situ* UHV-FTIR measurements were carried out in transmission mode.

Figure 4.7 shows the UHV-FTIR spectra during exposure to various amounts of N_2O . Spectrum A shows no absorption signals and corresponds to the IR spectrum of the clean sample. After exposure to $1 \cdot 10^{-6}$ mbar N_2O (spectrum B), three absorption signals appear in the range of $2220\text{-}2260 \text{ cm}^{-1}$ as well as two signals in the range of $1220\text{-}1340 \text{ cm}^{-1}$, which can be assigned to the symmetric and asymmetric stretching modes of both N- and O-bonded N_2O species adsorbed at the active sites of the $\text{Fe}_2(\text{dobdc})$ powder sample. The comparison of both regions shows a correlation of the two main peaks at $2247/1330 \text{ cm}^{-1}$ and $2228/1304 \text{ cm}^{-1}$ based on the intensity ratios. The third

peak at 2218 cm^{-1} only appears as a small shoulder and is assigned to an adsorbed N_2O at a minority active site. The adsorption geometry of this N_2O species is unclear. At higher dosages (spectra C, D and E), five signals appear in total in both regions. The main signals at $2247/1330\text{ cm}^{-1}$ and $2228/1304\text{ cm}^{-1}$ show similar increase during dosing and, therefore, the assumed correlation between the signals is verified. The origin of the three minor signals, which are redshifted with regard to the main peak, is not clear. However, these signals can be assigned to N_2O , since they only appear after N_2O dosing and are situated in a typical range for adsorbed N_2O . In addition, the appearance of three minor signals is in good agreement with the previously determined adsorption sites from the CO adsorption experiment. A possible reason for the appearance of more than two signals for O- and N-bonded N_2O can be explained by the structural properties of the MOF. Defects in the framework alter the surroundings of the active Fe(II) centers and, therefore, adsorbed N_2O at these defect affected sites should lead to at least one new signal in the IR spectrum.

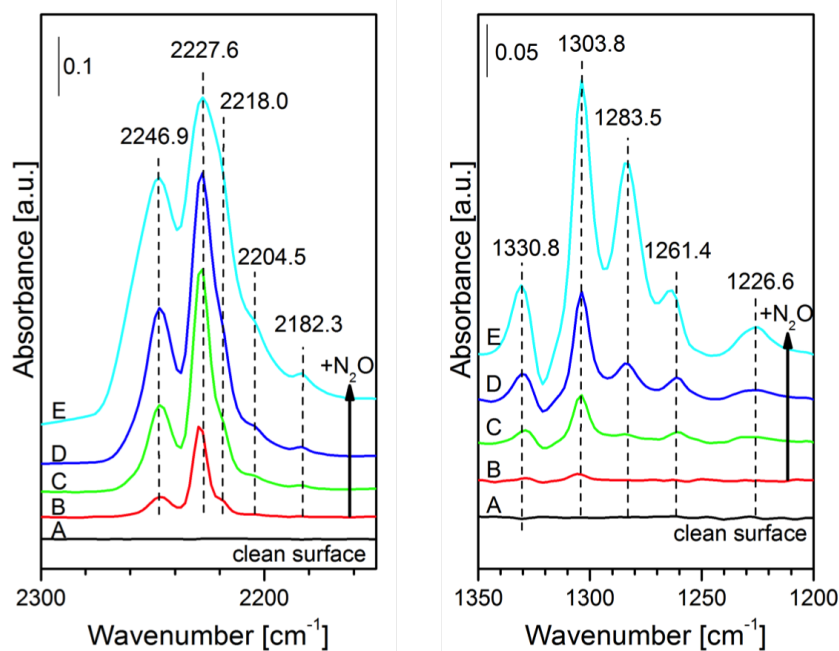


Figure 4.7: UHV-FTIR spectra of the $\text{Fe}_2(\text{dobdc})$ powder sample at 95 K during exposure to N_2O : (A) Clean surface, (B) $1 \cdot 10^{-6}\text{ mbar}$ N_2O for 7 min, (C) $5 \cdot 10^{-6}\text{ mbar}$ N_2O for 7 min, (D) $1 \cdot 10^{-5}\text{ mbar}$ N_2O for 7 min and (E) $5 \cdot 10^{-5}\text{ mbar}$ N_2O for 7 min.

The results show that N_2O adsorption of N_2O at the active centers of the metal-organic framework $\text{Fe}_2(\text{dobdc})$ gives two different pairs of signals in the typical range for N- and O-bonded N_2O . DFT calculations for N_2O adsorption at the active Fe(II) center of $\text{Fe}_2(\text{dobdc})$ ⁹ give binding energies of 45.6 and 44.5 $\text{kJ} \cdot \text{mol}^{-1}$ for the O- and N-bonded species, respectively. Therefore, the signals with the highest intensity at 2228/1304 cm^{-1} are assigned to O-bonded N_2O at the active Fe(II) center, as the O-bonded species should be energetically favoured over the N-bonded species. Hence, the N-bonded species is assigned to the pair of signals at 2247/1330 cm^{-1} . In addition, three minor signals assigned to minor adsorption sites appear during N_2O exposure. The IR spectra during annealing are shown in Figure 4.8. The data acquisition was carried out during the heating process, and the temperature was increased gradually.

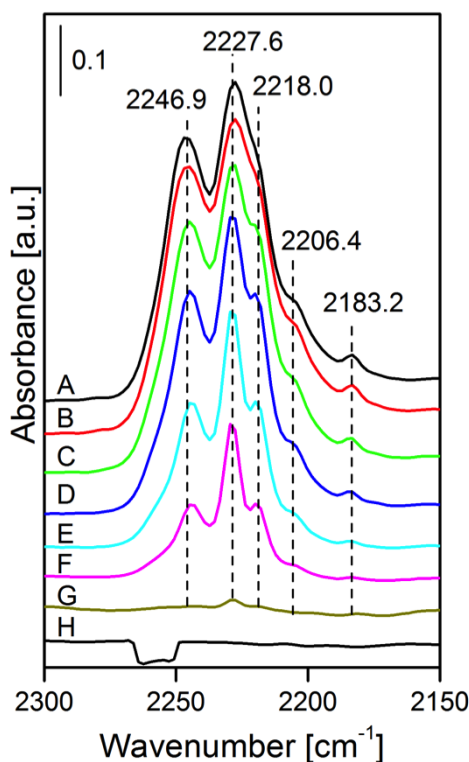


Figure 4.8: UHV-FTIR spectra of the $\text{Fe}_2(\text{dobdc})$ powder sample during annealing: (A) 98 K, (B) 102 K, (C) 108 K, (D) 113 K, (E) 120 K, (F) 143 K, (G) 168 K and (H) 194 K.

Upon heating, the intensity of the observed N_2O signals decreases due to desorption

of adsorbed N_2O and no additional signals appear in the whole measurement range (Fig. 4.8). The signal at 2183 cm^{-1} disappears at about 143 K (spectrum F). The other minor peaks at 2206 and 2218 cm^{-1} as well as the main peaks at 2228 and 2247 cm^{-1} decrease further, until only the main peak for the O-bonded N_2O species at 2228 cm^{-1} is visible at 168 K (spectrum G). At 194 K, the dosed N_2O is completely desorbed from the MOF (spectrum H) and the spectrum shows no signals for adsorbed N_2O on the sample. A comparison with the calculated binding energy from DFT measurements shows good agreement for the desorption process.⁴⁵ The O-bonded N_2O species has a higher binding energy and, therefore, more thermal energy is required to desorb the O-bonded species from the active center of the sample.

N_2O decomposition by the oxidation of the Fe(II) active center to a Fe(III)-hydroxy species, as proposed by Xiao et al.⁹, resulting in an additional signal for the Fe-OH stretching motion at 667 cm^{-1} has not been confirmed during this measurements. However, the dissociation of N_2O during the reaction can not be excluded and additional measurements with other analytic techniques, such as mass spectrometry, would have to be applied to detect the reaction products and distinguish between the possible reaction mechanisms.

5 Conclusion

5.1 Adsorbed N₂O on Rutile TiO₂(110)

The interaction of N₂O with an oxidized rutile TiO₂(110) single crystal has been studied by reflection-absorption IR spectroscopy under UHV conditions. After adsorption of N₂O on the TiO₂(110) surface, two signals appear in the IR spectra corresponding to the asymmetric $\nu_{NN}(N_2O)$ and the symmetric $\nu_{NO}(N_2O)$ vibrational modes of O-bonded N₂O on the rutile TiO₂(110) crystal surface, whereas no signals for the N-bonded species are found. The surface is fully saturated after low N₂O exposure and no increase in intensity has been observed at higher exposures. Heating the sample results in a decrease of the absorption signals, which deplete completely at around 135 K. In addition, UV irradiation of the surface after N₂O dosing leads to a depletion of the signals in the IR spectra. A correlation between irradiation time and N₂O decomposition has not been proven.

5.2 Adsorbed N₂O on Fe₂(dobdc)

The adsorption of CO and N₂O at the metal-organic framework Fe₂(dobdc) has been studied by transmission UHV-FTIR spectroscopy. The exposure of the sample to low amounts of CO result in a single signal in the IR spectrum assigned to the ν_{CO} stretching mode of CO adsorbed at active Fe(II) centers of the MOF. Higher amounts of CO result in the appearance of three additional adsorption sites, which can be assigned to absorption signals of CO bound to different defective sites of the framework. Upon heating, the minor peaks in the IR spectra deplete more quickly than the main peak, indicating a lower binding energy at the minority sites. However, determining the structure of this minority sites at the Fe₂(dobdc) powder sample was not possible by IR absorption experiments. Similar to CO, the exposure of the sample to N₂O results in a total of five bands in the range of the asymmetric $\nu_{NN}(N_2O)$ and the symmetric $\nu_{NO}(N_2O)$ stretching mode, respectively. Two of the signals in both regions show a correlated increase of the absorption signals and are assigned to the N- and O-bonded species at the active

metal centers. The other signals could not be assigned to a specific adsorption site, but in comparison with the CO dosing experiments, it is likely that these additional signals arise from minority active sites caused by defects in the molecular structure of the MOF.

References

- [1] Lashof, D. A.; Ahuja, D. R. *Nature* **1990**, *344*, 592–531.
- [2] Richter, R. D.; Caillol, S. *J. Photochem. Photobiol. C: Photochem. Rev.* **2011**,
- [3] Ravishankara, A. R.; Daniel, J. S.; Portmann, R. W. *Science* **2009**, *326*, 123–125.
- [4] Kudo, A.; Nagayoshi, H. *Catal. Lett.* **1998**, *52*.
- [5] Galle, M.; Agar, D. W.; Watzenberger, O. *Chem. Eng. Sci.* **2001**, *56*, 1587–1595.
- [6] Henderson, M. A.; Szanyi, J.; Peden, C. H. F. *Catal. Today* **2003**, *85*, 251–266.
- [7] Guarino, M.; Costa, A.; Porro, M. *Biores. Technol.* **2008**, *99*, 2650–2658.
- [8] Diebold, U. *Surf. Sci. Rep.* **2003**, *48*, 53–229.
- [9] Xiao, D. J. et al. *Nature* **2012**, *6*, 590–595.
- [10] Atkins, P. W.; de Paula, J. *Physikalische Chemie*, 4th ed.; Wiley-VCH, 2007.
- [11] Noei, H. Vibrational spectroscopic studies on adsorption and reactions over Zn-based catalysts. Ph.D. thesis, Ruhr-University Bochum, 2010.
- [12] Thimm, L. FT-IR und FT-NIR spektroskopische Untersuchungen in Kombination mit chemometrischen Auswertalgorithmen zur Charakterisierung der chemischen Zusammensetzung von Straßenbaubitumen. Ph.D. thesis, Universität Duisburg-Essen, 2009.
- [13] Meng, F. IR Spectroscopy Studies of Silver and Copper Nano-Films. Ph.D. thesis, Ruperto-Carola University of Heidelberg, 2007.
- [14] Kim, B.; Li, Z.; Kay, B. D.; Dohnálek, Z.; Kim, Y. K. *J. Phys. Chem. C* **2012**, *116*, 1145–1150.
- [15] Willeford, B. R. *Chem. Unserer Zeit* **1979**, *13*.

-
- [16] Haridas, R. P. *Anesthesiology* **2013**, *119*, 1014–1022.
- [17] Portmann, R. W.; Daniel, J. S.; Ravishankara, A. R. *Phil. Trans. R. Soc. B* **2012**, *376*, 1256–1264.
- [18] "Methane and Nitrous Oxide Emissions from Natural Sources". U.S. Environmental Protection Agency, Washington D.C., USA, 2010.
- [19] Kim, K. H.; Wanatabe, K.; Menzel, D.; Freund, H.-J. *J. Phys.: Condens. Matter* **2010**, *22*, 084012.
- [20] Rusu, C. N.; Yates, J. T. *J. Phys. Chem. B* **2001**, *105*, 2596–2603.
- [21] Obalová, L.; Reli, M.; Lang, J.; Matějka, V.; Kukutschová, J.; Kočí, K. *Catal. Today* **2013**, *209*, 170–175.
- [22] Lu, G.; Linsebigler, A.; Yates, J. T. *J. Phys. Chem.* **1995**, *99*, 7626–7631.
- [23] Malik, A.; Siddiqui, S. H. M. J.; Haque, M. M.; Muneer, M. *Int. J. Photoenergy* **2013**, *2013*, 768348.
- [24] Xu, M.; Gao, Y.; Moreno, E. M.; Kunst, M.; Muhler, M.; Wang, Y.; Idriss, H.; Wöll, C. *Phys. Rev. Lett.* **2011**, *106*, 138302.
- [25] Shaw, K.; Christensen, P.; Hamnet, A. *Electrochimica Acta* **1996**, *41*, 719–728.
- [26] Nadeen, M. Reactions of Ethanol on Bare and Noble Metal Modified TiO₂ Single Crystal and Powders. Ph.D. thesis, University of Auckland, 2012.
- [27] Menetrey, M.; Markovits, A.; Minot, C. *Surf. Sci.* **2003**, *524*, 49–62.
- [28] Calatayud, M.; Markovits, A.; Menetrey, M.; Mguig, B.; Minott, C. *Catal. Today* **2003**, *85*, 125–143.
- [29] Li, S.-C.; Diebold, U. *J. Am. Chem. Soc.* **2010**, *132*, 64–66.
- [30] Sorescu, D. S.; Rusu, C. N.; Yates, J. T. *J. Phys. Chem. B* **2000**, *104*, 4408–4417.

-
- [31] Diebold, U.; Li, S.-C.; Schmid, M. *Annu. Rev. Phys. Chem.* **2010**, *61*, 129–148.
- [32] Shultz, A. N.; III, W. M. H.; Baer, D. R.; Wang, L.-Q.; Engelhard, M. H. *Surf. Sci.* **1997**, *392*.
- [33] Oviedo, J.; Sanz, J. F. *J. Phys. Chem. B* **2005**, *109*, 16223–16226.
- [34] Rosi, N. L.; Kim, J.; Eddaoudi, M.; O’Keeffe, B. C. M.; Yaghi, O. M. *J. Am. Chem. Soc.* **2005**, *127*, 1504–1518.
- [35] Kaye, S. S.; Dailly, A.; Yaghi, O. M.; Long, J. R. *J. Am. Chem. Soc.* **2007**, *129*, 14176–14177.
- [36] Bloch, E. D.; Murray, L. J.; Queen, W. L.; Chavan, S.; Maximoff, S. N.; Bigi, J. P.; Krishna, R.; Peterson, V. K.; Grandjean, F.; Long, G. J.; Smit, B.; Bordiga, S.; Brown, C. M.; Long, J. R. *J. Am. Chem. Soc.* **2011**, *113*, 14814–14822.
- [37] Leclerc, H.; Vimont, A.; Lavalley, J.-C.; Daturi, M.; Wiersum, A. D.; Llwellyn, P. L.; Horcajada, P.; Férey, G.; Serre, C. *Phys. Chem. Chem. Phys.* **2011**, *13*, 11748–11756.
- [38] Queen, W. L. et al. *Chem. Sci.* **2014**, *5*, 4569–4581.
- [39] Kapelewski, M. T.; Geier, S. J.; Hudson, M. R.; Stück, D.; Mason, J. A.; Nelson, J. N.; Xiao, D. J.; Hulvey, Z.; Gilmour, E.; Fitzgerald, S. A.; Head-Gordon, M.; Brown, C. M.; Long, J. R. *J. Am. Chem. Soc.* *2014* **2014**, *136*, 12199–12129.
- [40] Millward, A. R.; Yaghi, O. M. *J. Am. Chem. Soc.* **2005**, *127*, 17998–17999.
- [41] Wang, Y.; Glenz, A.; Muhler, M.; Wöll, C. *Rev. Sci. Instrum.* **2009**, *80*, 113108.
- [42] Xu, M.; Noei, H.; Fink, K.; Muhler, M.; Wang, Y.; Wöll, C. *Angew. Chem. Int. Ed.* **2012**, *51*, 4731–4734.
- [43] Kim, B.; Li, Z.; Kay, B. D.; Dohnálek, Z.; Kim, Y. K. *J. Phys. Chem. C* *2014* **2014**, *118*, 9544–9550.
-

-
- [44] Noei, H.; Kozachuk, O.; Amirjalayer, S.; Bureekaew, S.; Kauer, M.; Schmid, R.; Marler, B.; Muhler, M.; Fischer, R. A.; Wang, Y. *J. Phys. Chem. C* **2013**, *117*, 5658–5666.
- [45] Stodt, D.; Noei, H.; Hättig, C.; Wang, Y. *Phys. Chem. Chem. Phys.* **2013**, *15*, 466–472.